Available online at www.sciencedirect.com
SCIENCE DIRECT®
International Journal of Mass Spectrometry 229 (2003) 117–142
International Journal of Mass Spectrometry
www.elsevier.com/locate/ijms

Review

Core level excitation, ionization, relaxation, and fragmentation of free clusters

Eckart Rühl*

Lehrstuhl für Physikalische Chemie I, Institut für Physikalische Chemie der Universität Würzburg, Würzburg D-97074, Germany

Received 16 May 2003; accepted 13 August 2003

Dedicated to Prof. Dr. Helmut Schwarz on the occasion of his 60th birthday

Abstract

Recent progress in the field of core level excitation of free clusters is reviewed, where size effects of the electronic and geometric structure in variable size clusters are investigated by element-selective excitation. Moreover, size-dependent changes in inner-shell photoionization, as well as electronic and radiative relaxation, and fragmentation of the doubly and multiply charged clusters are discussed. Model systems, that have been investigated to date, are primarily van der Waals clusters containing rare gases or simple molecules. More recently, clusters containing hydrogen-bonds, as well as covalent and ionic clusters have been investigated. These results are also included in this review as well as progress from theoretical studies.

Keywords: Core level excitation; Ionization; Relaxation; Fragmentation; Free clusters

1. Introduction

Size effects of matter have been of considerable interest in the past [1–4]. This is on one hand due to the fundamental interest in structural changes by going from the gas to macroscopic condensed matter. On the other hand, size-dependent changes of free and deposited clusters as well as nanoscopic matter give clear perspectives to applied research, such as materials science, where numerous properties of clusters and particles, such as their optical, magnetic, and dynamical changes as a function of size and composition, have been investigated with respect to possible applications [5–9].

The strongest changes in electronic structure of variable size matter are found, when the isolated atom is compared to microclusters [3]. Finally, the electronic properties gradually merge into those of macroscopic condensed matter with increasing cluster size. On the other hand, even in variable size nanoparticles, one observes size-dependent changes of the optical properties [10].

Various experimental and theoretical approaches have been used in the past in order to investigate size effects of matter in a systematic way. Some experiments rely on ionization in combination with mass spectrometry [3]. Others involve the excitation of outer electronic shells [11–14], which reflect changes in bonding. These levels may already correspond to inner-shell excitations, if heavy elements are investigated [15]. Besides photoexcitation, inelastic scattering of electrons has been used to investigate structural changes as a function of cluster size [16].

Core level excitation involves the excitation deeply of bound electronic shells. These belong in the case of light elements to K- or L-shells, corresponding to the excitation of electrons in 1s-, 2s-, and 2p-orbitals. The excitation of core levels requires substantially higher photon energies than are needed for the excitation of outer electronic shells, so that, e.g., photon excitation in the soft or hard X-ray regime or inelastic collisions with high kinetic energy electrons are required. The binding energies of core electrons are element-specific [17]. Small changes in excitation energy may occur as a result of the local surroundings of the excited atom, which may change the properties of the initial and final states [18]. In conventional X-ray photoelectron spectroscopy (XPS or ESCA [19]), such ‘chemical shifts’ can

* Tel.: +49-931-888-6300; fax: +49-931-888-6302.
E-mail address: eruehl@phys-chemie.uni-wuerzburg.de (E. Rühl).

1387-3806/$ – see front matter © 2003 Elsevier B.V. All rights reserved.
doi:10.1016/j.ijms.2003.08.006

be measured by small changes in kinetic energy of the photoelectrons [18]. Their magnitude is substantially smaller than the excitation energy. Alternatively, the local electronic structure can also be probed by inner-shell absorption or related approaches, such as inner-shell electron energy loss spectroscopy, where transitions of core electrons into unoccupied electronic levels are investigated [20]. The primary excitation of a core electron into an excited electronic state leaves a core hole that is immediately filled by electronic or radiative relaxation processes, as probed recently in real time by attosecond laser pulses [21]. The detection of core electrons is also known to give specific information on structural properties of the sample [22]. Furthermore, specific information on the local geometrical structure of matter is obtained from the single and multiple scattering of the photoelectron at its neighbors, which is commonly known as 'extended X-ray absorption fine structure' (EXAFS [23]). Numerous samples of condensed matter and some gas phase molecules have been investigated by this technique.

This wealth of experimental approaches already indicates that core level excitation is expected to be a sensitive method to study size effects of matter. However, the field of core level excitation of free clusters has developed in the last decade [24]. This is mostly due to the fact that free clusters in the gas phase are typically formed highly diluted in jet expansions. High intensity X-ray sources are required in order to perform equivalent experiments to macroscopic condensed matter, which is investigated since decades by X-ray spectroscopies. Suitable photon sources for site-specific structural research are tunable in photon energy, where most commonly synchrotron radiation is used [25]. As a result, X-ray absorption or related experiments, that probe size effects in electronic structure, can be performed. Studies on free clusters require high brilliance synchrotron radiation, which has become available during the last years. Both, recent progress in new synchrotron radiation facilities and compact, high intensity jet experiments were the key, that gave new insight into size effects of matter that are probed by element-specific core level excitation in free variable size clusters.

We review recent progress in this field, where size effects in electronic and geometric structure are discussed for simple model systems, such as van der Waals clusters and other prototype cluster systems containing ionic, covalent, and hydrogen bonds. These show the potential of this approach for applications to fundamental and applied research. Moreover, we discuss size effects in inner-shell photoionization and relaxation. Finally, fragmentation of the doubly and multiply charged clusters is discussed in detail. Perspectives for future research are presented at the end of this review.

2. Experimental

Variable size clusters in the gas phase are efficiently produced in adiabatic expansions of neat gases or gas mixtures into the vacuum [3]. A small nozzle of typically 10–100 μm diameter is used to expand the gases. The size distribution of neutral clusters that are formed in jet expansions is reflected by log-normal distributions [26]. They are characterized by the average cluster size $\langle N \rangle$, which can be estimated from scaling laws. These contain scaling parameters, which were introduced for atomic clusters by Hagena [27]. Later work also allowed to estimate the average cluster size of molecular van der Walls clusters [28]. The advantage of this approach is, that various experimental quantities, that characterize a jet expansion, such as the stagnation temperature T_0, the stagnation pressure p_0 in the high pressure reservoir, the nozzle diameter d, and its shape, are combined to a reduced scaling parameter Γ^* that can be related to $\langle N \rangle$. Further details on the calculation of Γ^* for various atomic clusters can be found in [27]. Several experimental studies were concerned with the correlation of both quantities. These include electron diffraction [16], mass spectrometry [29], and molecular beam scattering experiments [30]. The latter approach is especially suitable for small clusters. The typical $\langle N \rangle$-range that is covered by most experiments devoted to core level excitation, reaches from the isolated gas phase up to several thousand atoms per cluster. Table 1 gives an overview on the correlation of Γ^* with $\langle N \rangle$.

We note that there are other approaches for cluster formation, such as the pick-up of condensable gases on rare gas clusters or the evaporation of low volatile compounds in oven sources (cf. [3]).

The jet is skimmed, so that the clusters are reaching the adjacent detection chamber. There, it is intersected with a beam of monochromatic synchrotron radiation. The interaction region is typically located in the ionization region of a time-of-flight mass spectrometer or a photoelectron spectrometer (cf. [31–33] and Section 3.3).

Table 1
Correlation of Γ^* with $\langle N \rangle$ for argon clusters, when $p_0 = 5$ bar of argon are expanded through a 50 μm nozzle

T_0 (°C)	Γ^*	$\langle N \rangle$[a]	$\langle N \rangle$[b]
30	490	10	10
0	620	15	20
−10	675	18	30
−20	740	20	50
−30	810	22	80
−40	900	25	105
−50	990	35	140
−60	1100	40	175
−70	1230	50	225
−80	1380	60	270
−90	1570	70	340
−100	1790	80	430
−110	2050	120	530
−120	2310	200	750

The stagnation temperature T_0 is measured at the nozzle tip. Γ^* is calculated according to [27]. The correlation of Γ^* with $\langle N \rangle$ is obtained from [29] and [16], respectively.
[a] From [29].
[b] From [16].

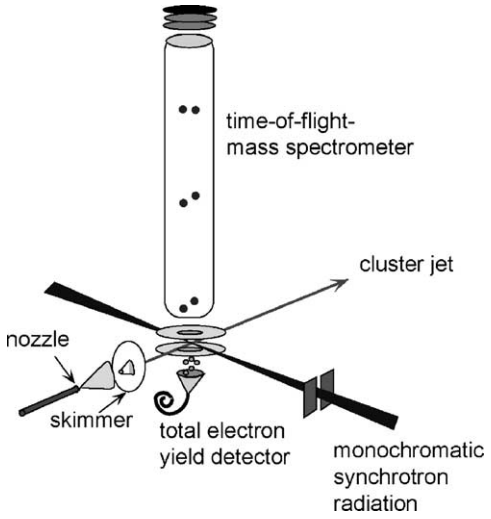

Fig. 1. Schematic diagram of an experimental setup that is suitable for core level excitation of free clusters. The detectors (time-of-flight mass spectrometer and total electron yield detector) can be replaced by other devices (see text for further details).

The experiments, that have been carried out in the field of core level excitation, made use of compact portable jet expansion setups (see Fig. 1). These are flexible in use and easy to mount in short time periods at storage ring facilities [32,34–36]. This is different from earlier approaches, where large molecular beam end stations were permanently installed at normal incidence or grazing incidence beam lines, which gave numerous results on outer-shell excitation of clusters [12,13,37].

Cations are detected either in a total ion yield mode or mass spectra are recorded at constant photon energy. Alternatively, photoion yields of mass-selected cations are measured as a function of photon energy. Time-of-flight mass spectrometers are more suitable than quadrupole mass spectrometers for such experiments, since their mass range is not limited and photoion yields of numerous selected cation channels can be measured simultaneously under entirely identical conditions with high transmission for various kinetic energy cations. As a result, very small energy shifts between selected mass channels can be measured by photoion yields as a function of photon energy. These shifts can be as small as 1–2 meV in the soft X-ray regime, if high resolution monochromators are available [38]. The length of the field free drift region of the time-of-flight mass spectrometer is of crucial importance to the efficient detection of cations. Most favorably, short flight tubes are used so that the cation flight time is compatible with the time structure of the storage ring [29,39]. Recent work shows that repetition rates up to 1 MHz can be handled with short time-of-flight mass spectrometers, which have constant extraction voltages with sufficient electrical field strength to accelerate and focus the ions onto the detector [36]. An inherent drawback of this approach is the limited mass range, so that preferably small clusters are investigated. Small circumference storage rings with higher repetition rates require to use pulsed cation extraction from the ionization region. Typical repetition rates of the cation extraction pulse are of the order of 30–50 kHz [31]. This allows to measure longer cation flight times, which are essential in the case of the detection of heavy cluster masses with high mass-to-charge ratios ($m/z > 10^3$) as well as accurate kinetic energy releases that come from the cation decay of doubly and multiply charged clusters [31].

Electrons can be detected simultaneously with cations, if they are extracted into opposite direction, so that, e.g., total electron yields (TEYs) are detected [32]. Note that total electron yield detectors, consisting just of a channeltron, detect often less efficiently high kinetic energy Auger electrons than slow electrons [40]. In addition, the simultaneous detection of cations and electrons permits multicoincidence experiments between photoelectrons and photoions, such as photoelectron–photoion coincidence spectroscopy (PEPICO) [41] or photoelectron–photoion–photoion coincidence spectroscopy (PEPIPICO) [42–44]. More recently, high resolution photoelectron spectroscopy experiments have been performed, where electrostatic electron energy analyzers were used [45–47]. Alternatively, tunable radiation allows the detection of slow electrons, such as threshold photoelectrons [48] or zero kinetic energy (ZEKE) photoelectrons [49]. Threshold photoelectrons are detected by accelerating the electrons in a constant electric field of a few V/cm from the ionization region into the electron spectrometer, where angular discrimination suppresses the energetic electrons that are simultaneously formed. In contrast, ZEKE electrons are separated from kinetic electrons, such as Auger electrons, in a field free ionization region. Subsequently, the ZEKE electrons are extracted by a delayed, weak voltage pulse into the electron spectrometer, where they are identified by their flight time.

Fluorescence spectroscopy has also been used in core level excitation experiments on clusters. Electronically excited fragments are formed, so that radiative relaxation in the ultraviolet or vacuum ultraviolet (VUV) regime can be detected [50], similar to experiments on valence shell excitation [29]. Fluorescence excitation spectra as well as dispersed fluorescence spectra at constant excitation energy can be measured with such setups.

The decay mechanisms of singly and multiply charged clusters are commonly measured by various coincidence techniques, involving the simultaneous detection of electrons and ions [31,41,43,51]. The flight time measurements of time-correlated charged products from clusters are commonly started with the arrival of an electron, which provides the start signal for a time-to-amplitude converter or a time-to-digital converter. Single cation stops lead to PEPICO spectra. In PEPIPICO spectroscopy, two correlated cations from the same multiply charged cluster stop the flight time measurements. Three stops from time-correlated cations from the same at least triply charged cluster are required in photoelectron–photoion–photoion–photoion coincidence (PEPIPIPICO) spectroscopy.

3. Results and discussion

We discuss in the following typical results on the electronic structure of variable size clusters that have been investigated by core level excitation. Section 3.1 is followed by a brief discussion on investigation on the electronic structure of clusters using the EXAFS (see Section 3.2). Subsequently, recent results on core level photoionization, electronic and radiative relaxation, as well as fragmentation of free clusters are presented.

3.1. Electronic structure

3.1.1. Atomic van der Waals clusters

Until about a decade ago, the highest energy excitation of free van der Waals clusters was performed in the Ar 3s regime [52], i.e., in the inner-valence regime below 30 eV photon energy, where changes in the Rydberg/exciton structure were investigated for dimers and trimers. First experiments and theoretical models on free core-excited atomic van der Waals clusters were focused on the Ar 2p-excitation of variable size argon clusters [31,32,35,36,44,53–56]. Primary motivation of this work came initially from already known changes in electronic structure between the atomic absorption cross section and that of the solid [57,58]. These changes occur in the near-edge regime as a result of the occurrence of core-excitons in the solid, which are shifted to higher energy relative to the atomic Rydberg states. Early low resolution work on free, variable size clusters provided systematic changes of the Ar $2p_{3/2} \rightarrow 4s$ surface- and bulk-excitons, which could initially not be resolved. Later high resolution work on neon and argon clusters gave detailed insight into the size-dependent energy shifts of these surface and bulk excitons [33,36]. These energy shifts were assigned in terms of compressed final states by the surrounding atoms, resulting in an overall blueshift of the surface and bulk states, which increases with increasing coordination number of the absorbing atom [36]. We will not discuss in the following these results in greater detail. It will rather be shown a very clear example, which is represented by the Kr 3d excitation (90–100 eV). This absorption edge has the inherent advantage that it is located at fairly low excitation energy: high energy resolution is provided by soft X-ray monochromators and there is small natural line broadening, which comes essentially from the lifetime of the core hole. This allows one to measure small energy shifts as a function of the average cluster size [40].

Fig. 2 shows a comparison of the absorption cross section of gaseous and solid krypton near the Kr 3d-edge (cf. [58]). The gas phase spectrum shows two *n*p-Rydberg series. They arise from spin-orbit splitting and converge to the Kr $3d_{5/2}$- and Kr $3d_{3/2}$-series limits at 93.80 and 94.00 eV, respectively [59], where the convergence limits are marked by vertical arrows. In contrast, the corresponding features in the condensed phase spectrum are broader in width and shifted to higher photon energy, reflecting considerable changes in electronic structure from the gas to the condensed phase. The size-dependent evolution of the lowest energy transition in the Kr 3d regime (Kr $3d_{5/2} \rightarrow 5p$) is shown in greater detail in Figs. 3 and 4 [40]. The atomic transition is represented by a single Voigt profile, where the Lorentzian contribution clearly dominates ($\Gamma = 95$ meV), so that Lorentzian line shapes can be used for spectral de-convolutions [40]. This line width is essentially due to the life time of the Kr 3d core hole [18].

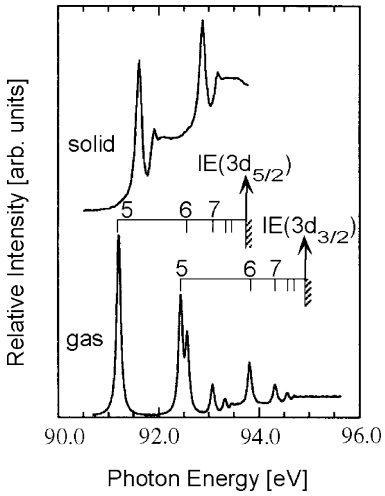

Fig. 2. Comparison of the near-edge absorption of gaseous (atomic) and solid krypton in the Kr 3d-excitation regime. Rydberg series converging to the Kr 3d ionization energies ($3d_{5/2}$ and $3d_{3/2}$) are indicated by vertical arrows. The principal quantum numbers *n* of low-lying *n*p-Rydberg states are shown.

Changes in electronic structure of small clusters are investigated by photoion yields of mass-selected cluster cations, such as Kr_2^+ (see Fig. 3), where photoion yields of larger cations, e.g., Kr_3^+, give similar results, but their intensity

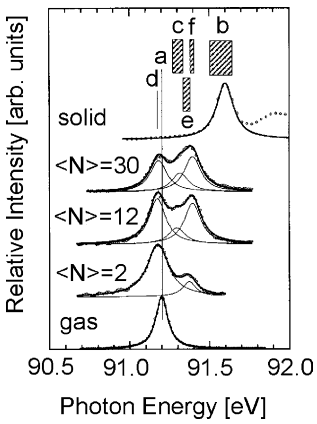

Fig. 3. Detailed view on the evolution of the Kr $3d_{5/2} \rightarrow 5p$-transition in gaseous krypton (bottom), variable size clusters (middle), and solid krypton (top). The spectra of variable size clusters are obtained from the Kr_2^+-yield, which was recorded at different values of the average cluster size $\langle N \rangle$. The shaded areas correspond to calculated transition energies of atoms that are bound at different sites in a cluster, with d: dimer, a: atom, c: corner, e: edge, f: face, b: bulk. See text and [40] for further details.

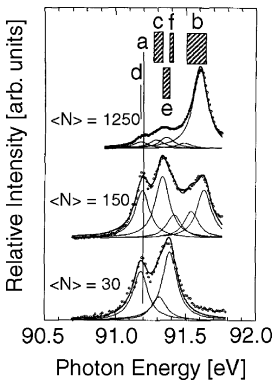

Fig. 4. Detailed view on the evolution of the Kr $3d_{5/2} \rightarrow 5p$-transition of variable size clusters. The spectra are obtained from total electron yields [40].

is considerably weaker, so that these results are not discussed. The Kr_2^+-channel is populated via fragmentation of the singly and multiply charged clusters via ionic cluster fragmentation of larger neutral clusters, as will be shown in Section 3.5. Variations of $\langle N \rangle$ change the Kr_2^+-yield, if the cluster size is below the critical cluster size of fission of Kr_n^{++}, where $n = 71$ [60] (see also Fig. 3). This implies that larger doubly charged clusters do not decay efficiently into the mass channels of small, singly charged fragments.

The jet is dominated by atoms near the threshold of cluster formation, corresponding to $\langle N \rangle \approx 2$. The weak Kr_2^+-signal comes mostly from neutral dimers (Kr_2) and there are contributions from somewhat larger clusters Kr_n ($n \geq 3$), which are also present in the size distribution at $\langle N \rangle = 2$. These contributions are reflected by the shape of the Kr_2^+-yield near the lowest energy transition ($Kr_{5/2} \rightarrow 5p$). The maximum is slightly redshifted, i.e., shifted to lower energy by ≈25 meV relative to the atomic transition (cf. Fig. 3) [40]. The line width is somewhat increased, which indicates that there are other line broadening processes besides the core hole life time. This additional broadening is likely due to short-lived final states in krypton clusters. Besides the dominant redshifted feature, there is also a weak blueshifted shoulder in the Kr_2^+-yield at $\langle N \rangle = 2$ (cf. Fig. 3), which is assigned to fragmentation of larger cluster cations into the selected Kr_2^+-channel. This assignment is consistent with the spectral evolution with increasing $\langle N \rangle$, where the blueshifted feature grows in intensity. This is due to fragmentation of larger clusters into the Kr_2^+-channel. As a result, photoion yields of mass-selected cluster cations, such as Kr_2^+, are suitable to detect changes in electronic structure of core-excited neutral clusters with the inherent advantage that the dominant atomic contribution to the jet in the low $\langle N \rangle$-regime is efficiently suppressed by this approach.

The evolution of the Kr_2^+-signal with $\langle N \rangle$ is deconvoluted by Lorentzian profiles. Up to three components are required to obtain a reasonable fit to the experimental results (see Fig. 3). Besides dimers, three surface components are tentatively assigned to corner-sites (c), edge-sites (e), and face-sites (f). These surface excitons are expected to absorb at increasing energy, according to earlier work [61,62]. Bulk-sites (b) are not expected to occur in small clusters, because of their high surface-to-bulk ratio [63]. This assignment is confirmed by model calculations [40] which are based on the non-structural core exciton theory of Resca et al. [64], indicating that different geometric sites in clusters give rise to characteristically shifted transition energies relative to the bare atom, as indicated in Fig. 3 (shaded areas) [40].

The dimer absorption is expected to occur at lower energy than the atomic transition, which is due to the dominant polarization shift, which always gives rise to a redshift relative to the atomic absorption line [61,62]. Atoms that are located either at various surface- or bulk-sites are expected to give blueshifted resonances, which result from screening. The competition between screening of the electron, due to repulsive scattering, and the increased electron binding, due to cluster polarization, determines the overall sign of spectral shift relative to the atomic transition. Considerably larger blueshifts than for surface sites are expected for subsurface atoms and atoms that are located deep in the bulk of the clusters, leading to blueshifts ≥400 meV [40]. The model calculations consider firstly perfectly shaped clusters of icosahedral geometry [63], which represent the lowest energy structures of small krypton clusters, as well as other rare gas clusters with the exception of helium clusters. In addition, imperfectly shaped isomers are considered, which are somewhat lower in stability. However, the difference in energy between perfect and imperfect structures is known to be small [63,65], so that various isomers are expected to occur in the jet. The geometric structure of clusters has two different effects on the shape of the near-edge transitions:

(i) The absorption energies of the various surface- and bulk-sites depend on the local structural and electronic surroundings. Therefore, one finds instead of a single, well-defined transition energy of a geometric site an energy region, in which an atom absorbs that is bound at a certain geometric site. This corresponds to the hatched areas in Fig. 3.

(ii) The relative intensities of the different surface- and bulk-sites depend strongly on the geometric structure of the cluster. Imperfectly shaped clusters are expected to be dominated by edge-sites, whereas face- and bulk-sites should be stronger in perfectly shaped icosahedral or cuboctahedral clusters.

The relative intensities of the $Kr_{5/2} \rightarrow 5p$-transitions give an estimate on the relative occurrence of the individual sites in variable size Kr clusters. The experimental results indicate that the local surroundings of the absorbing atom is of crucial importance to the energy of the transition. Fig. 3 shows that mostly imperfectly shaped clusters are formed in the jet expansion, where edge-sites dominate the surface component with increasing $\langle N \rangle$ and there are only weak contributions from corner-sites. Bulk and face sites are not ob-

served in the low $\langle N \rangle$ regime, even though one would expect already at $\langle N \rangle = 13$ that one atom is located in the bulk, if this cluster consists of a perfect icosahedron. Kr_{13} is expected to have already 8% of its atoms in the bulk, whereas for the next shell, corresponding to Kr_{55}, the contribution of bulk sites increases to 24% [63]. From the experimental results, shown in Fig. 3, it becomes evident that there are no bulk features, even at $\langle N \rangle = 30$. First evidence for transitions of bulk sites occurs at $\langle N \rangle > 100$, which is clear evidence for considering the occurrence of imperfect cluster structures, with a considerably enhanced surface-to-bulk ratio (cf. Fig. 4). However, it is not possible to assign a single cluster structure to the spectral features, since there is a distribution of various cluster sizes and shapes present in the jet at a given $\langle N \rangle$.

The Kr_2^+-yield decreases and finally vanishes, if $\langle N \rangle$ is further increased, indicating that fragmentation of large clusters does not support the formation of small fragment ions above the critical size of stable doubly and multiply charged clusters [66], where the stability limit of stable doubly charged Kr-clusters is $\geq$71 atoms per cluster [60].

Total electron yields are a suitable alternative to investigate changes in electronic structure in the high $\langle N \rangle$-regime, where the mixing ratio of clusters becomes large compared to the atomic contribution. Fig. 4 shows the continuation of the size evolution in the large $\langle N \rangle$-regime, where the atomic contribution has been subtracted in order to observe exclusively size-dependent changes in electronic structure of clusters as a function of $\langle N \rangle$. The reliability of this approach is demonstrated by comparing the TEY corresponding to $\langle N \rangle = 30$ to the Kr_2^+-yield recorded at the same average cluster size. The comparison indicates that both experimental approaches give similar results. Clear evidence for two different bulk sites, corresponding to a sub-surface layer and atoms that are located deeper in the bulk, is found at $\langle N \rangle = 150$, where edge sites are still the dominant spectral component. Finally, in the large cluster limit, bulk sites dominate.

The example of variable size krypton clusters indicates that systematic, size-dependent changes in electronic structure are tightly related to the geometric structure in van der Waals clusters. An alternative approach to obtain directly structural information on free van der Waals clusters is outlined in Section 3.2, where results from EXAFS spectroscopy are discussed.

3.1.2. Molecular van der Waals clusters

Numerous molecular van der Waals clusters have been investigated in the core-level regime [38,44,54,67–72]. Early work in this field relied on low spectral resolution in the near-edge regime, where hardly any size-dependent changes in electronic structure were observed [67]. Substantial broadening as well as energy shifts occur in the molecular Rydberg/exciton regime, similar to rare gas clusters (see Section 3.1.1). Moreover, heterogeneous van der Waals clusters, containing rare gases and molecular moieties were studied by element-specific excitation [44]. These undergo composition-specific energy shifts of exciton lines near the rare gas absorption edges, as evidenced for N_2/Ar-clusters. The blueshifts are found to be greater than in homogeneous rare gas clusters and they are comparable in magnitude to the corresponding condensed gas mixtures [73]. We will not discuss this early work in detail and focus rather on recent examples of high resolution near-edge spectroscopy, where small but distinct changes between isolated and clustered molecules become visible. This progress relies on high resolution beam lines which have become available during the last years. The following Sections 3.1.2.1–3.1.2.3 on molecular van der Waals clusters are primarily devoted to high resolution work on core-to-valence transitions. We also show results on hydrogen bonded clusters (see Section 3.1.2.4), ionic clusters (Section 3.1.2.5), and covalent clusters (Section 3.1.2.6).

3.1.2.1. Nitrogen clusters. Fig. 5 shows a comparison of the near-edge structure of free and clustered nitrogen near the lowest energy transition in the N 1s regime, corresponding to the N 1s $\rightarrow$ π^*-transition [71]. The shape of the N 1s $\rightarrow$ π^*-transition is well-known [74,75]. It consists of a Franck–Condon progression that extends to $\nu' = 6$. The photoion yield of N^+ reflects the molecular properties, since molecular nitrogen is the primary source of this cation. The electronic properties of clustered nitrogen are obtained from the photoion yield of $(N_2)_2^+$. This cation is efficiently formed as a fragment from larger clusters. The average cluster size $\langle N \rangle \approx 150$ is estimated according to earlier work [28].

Both spectra shown in Fig. 5 are almost identical in shape and energy position, so that changes in electronic structure as a function of $\langle N \rangle$ are not as evident as in the case of the conversion of atomic Rydberg transitions into the corresponding surface and bulk excitons (see Section 3.1.1).

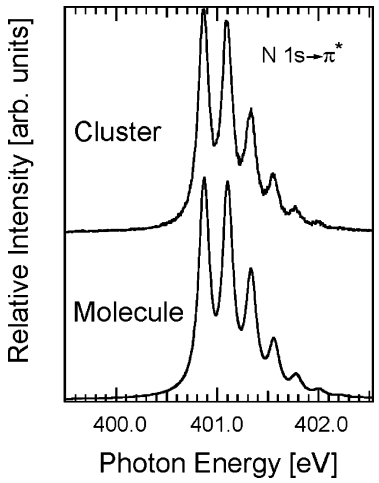

Fig. 5. Comparison of the N 1s $\rightarrow$ π^*-band in molecular nitrogen and nitrogen clusters at $\langle N \rangle \approx 150$. The molecular spectrum is obtained from the N^+-yield, the cluster spectrum comes from the $(N_2)_2^+$-yield [71]. Both spectra have been measured simultaneously.

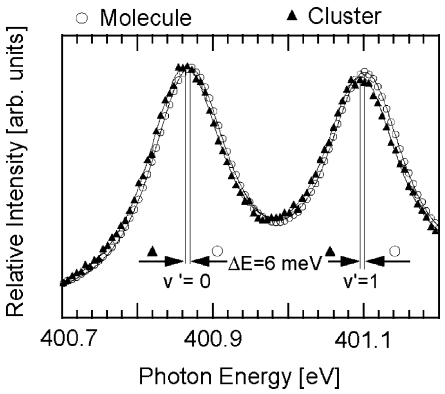

Fig. 6. Detailed view on the low energy portion of the N 1s → π*-band near $\nu' = 0$ and $\nu' = 1$ for molecular and clustered nitrogen [38,71]. See text and Fig. 5 for further details.

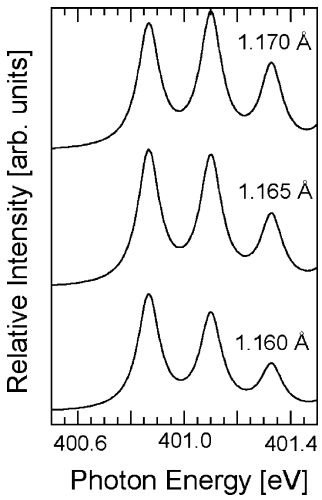

Fig. 7. Calculated Franck–Condon structure of N 1s → π*-excited nitrogen. The transitions are broadened by Voigt-profiles in order to obtain resemblance with the experimental data (cf. Figs. 5 and 6). See text and [38] for further details.

This result is in accordance with earlier low resolution work, where the spectral resolution was not sufficient to resolve any energy shifts and vibrational fine structure at all [67,76].

Fig. 6 shows a portion of the vibrationally resolved N 1s → π* ($\nu' = 0$, 1)-transition of molecular and clustered nitrogen. A comparison between the pure gas and clusters indicates that there are only small, but distinct differences between both spectra. These include a small redshift of the N 1s → π*-transition of clusters relative to the bare molecule as well as small changes in Franck–Condon factors, where the intensity of the levels $\nu' > 0$ is slightly reduced relative to the vibrational ground state level ($\nu' = 0$). We do not observed any spectral broadening in clusters relative to the isolated molecule, which is unlike the results on the size-dependent evolution of the Rydberg-states in Kr-clusters (see Section 3.1.1). Various possible origins of this small redshift have been discussed before [71]. Freezing of molecular rotations due to the formation of a solid cluster can only lead to a small blueshift rather than to a redshift. Similarly, changes in intramolecular bonding were discounted in previous work [71]. It was rather assumed that intermolecular vibrations are the origin of the redshift along with dynamic localization, as will be outlined in greater detail in Section 3.1.2.3.

Changes in the relative intensities of the bands within the 1s → π* progression are assumed to be governed by small changes in local geometry of the core-excited molecules that are bound in clusters. Thus, the relative enhancement of the $\nu' = 0$-level in clusters is rationalized by a decrease of the intramolecular equilibrium distance r_e upon N 1s-excitation. Changes in Franck–Condon factors in clusters have been modeled by using a Morse potential energy function for the $^1\sum_g{}^+$ ground state and the core-excited N 1s → π*-state [38]. This is similar to earlier work on the isolated molecule (cf., e.g. [74]). The observed vibrational constant ($\omega_e = 235.2\,cm^{-1}$) and anharmonicity constant ($\omega_e x_e = 1.9\,cm^{-1}$) are used to construct the Morse function of the excited state. The overlap integrals of the corresponding wave functions are evaluated numerically. The ground state equilibrium geometry and vibrational constants are taken from [77]. Slight variations of the excited-state N≡N distance change significantly the intensities of the vibrational bands (see Fig. 7). A variety of excited-state N≡N distances were used for the Franck–Condon calculations, ranging from $1.170\,Å \leq r_e \leq 1.160\,Å$, as shown in Fig. 7. Best agreement with the experimental results on clusters is obtained, if the intramolecular N≡N distance is slightly reduced by ∼100 fm relative to that of the bare molecule (cf. Fig. 5 and [71]), yielding for clustered nitrogen $r_e = 1.164\,Å$. This indicates that the strength of the intramolecular bond is slightly increased in N 1s-excited nitrogen that is bound in clusters.

3.1.2.2. Carbon monoxide clusters. The spectral shape of the C 1s → π*-transition of carbon monoxide clusters is obtained from the $(CO)_2{}^+$-yield at $\langle N \rangle \approx 150$ using the size estimate outlined in the previous section [28] (cf. Fig. 8). It is remarkably similar to the C 1s → π*-band of the isolated molecule, which is obtained from the O^+-yield. These results are consistent with those on N 1s-excited nitrogen clusters (cf. Section 3.1.2.1). The simultaneous measurement of photoion yields of the free molecules and clusters under entirely identical conditions allows us to identify small spectral shifts that can be as small as 1 meV (cf. [72]). The Franck–Condon factors are essentially unchanged in CO and its clusters. This is an indication for the fact that the C 1s → π*-transition is primarily governed by intramolecular properties rather than by weak intermolecular interactions. Moreover, the geometry changes are even smaller than in core-excited nitrogen clusters. However, there are small, but characteristic differences between the C 1s → π*-transitions in molecular CO and its clusters, which are different from the findings on nitrogen clusters. The $(CO)_2{}^+$-yield shows a characteristically broadened C 1s → π* ($\nu' = 0$)-transition, where 113 ± 1 meV are found in FWHM (cf.

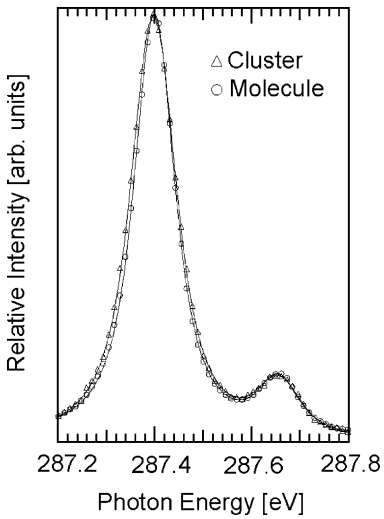

Fig. 8. Comparison of the C 1s → π*-band in molecular carbon monoxide and carbon monoxide clusters at ⟨N⟩ ≈ 150. The molecular spectrum is obtained from the O^+-yield, the cluster spectrum comes from the $(CO)_2{}^+$-yield [38]. Both spectra have been measured simultaneously.

Fig. 8). It is somewhat broader than the molecular transition (102 ± 1 meV). The band is approximated in both cases by a Voigt profile. The Lorentzian and Gaussian line widths are slightly increased in clusters, reaching 90 ± 1 meV and 50 ± 1 meV, respectively [72]. In contrast, one observes for the molecular transition 85 ± 1 meV and 41 ± 1 meV, respectively. The increased Gaussian width may be due to phonon-like broadening, as proposed in [38,72]. Further details on the assignment of the spectral shifts and changes in line widths will be outlined in the following section. In addition to changes in line profile, we observe a small, but clearly identifiable redshift of 2 ± 1 meV of the maximum of the C 1s → π* ($\nu' = 0$)-transition in clusters relative to the bare molecule. This spectral redshift can be as large as 4 ± 1 meV if molecular rotations are considered to be entirely frozen, as outlined in greater detail by Flesch et al. [38]. The origin of these spectral shifts is discussed in the following section (see Section 3.1.2.3).

3.1.2.3. Assignment of the spectral shifts and changes in line width in core-to-valence transitions of molecular van der Waals clusters. The increased Lorentzian line widths that are found in CO-clusters are unlikely the result of changes in the core-hole life time [38,71]. It is rather expected that they are efficiently affected by fast cluster decay dynamics of the final states, similar to atomic clusters (see Section 3.1.1). These final states are accessed in molecular clusters due to the intermolecular co-ordinate and partially by the presence of intermolecular vibrations Ω_N. At $N \rightarrow \infty$, the conventional picture of Gaussian broadening of X-ray transitions in solids is reached, with the standard deviation $\sigma = [S(\Omega)\mathrm{cotan}(\Omega/kT)]^{1/2}$, where the coupling constant S is equal to mean number of phonons Ω created in the transition, k is the Boltzmann constant, and T is the absolute temperature [38]. The increase of the Gaussian width by ≈20% gives evidence for phonon-like broadening in clusters. In general, X-ray transitions in clusters are strongly localized within the excited molecule, so that the spectral shift can either be assigned to efficient freezing of molecular rotations or a polaron-like shift of the Frank–Condon transition in defect centers [38]. A polaron-like shift can also account for dynamic stabilization, corresponding to a spectral redshift, of a core-excited molecule in a cluster [71]. This effect results from self-trapping in displaced positions off the equilibrium position in a shallow intermolecular potential of a deformable cluster, which is due to changes in the radius of interaction between the core-excited molecule and its neighbors in clusters and in the solid. Hence, an increase in dynamic stabilization on intramolecular vibrational bands (librations) is expected to occur, if the interaction of the core-excited molecule with its neighbors increases. Recent results on 1s-excited N_2-clusters give evidence for strong dynamic localization of the core hole in one of the equivalent atomic sites, since the dynamic dipole moment of core-excited nitrogen ($N_2{}^*$) will dominate the interaction with its neighbors [71]. The magnitude of the redshift is expected to be related to stabilization that occurs via the excitation of librations. In the case of CO-clusters there are no equivalent atomic sites, so that stabilization is expected to be negligible, resulting in a smaller redshift of the 1s → π*-transition than in N_2-clusters [38].

Finally, we note that substantial blueshifts of the order of 1 eV are observed for core-to-valence transitions occurring in core ionization continua, such as 1s → σ*-transitions of clusters containing homonuclear diatomic molecules, such as N_2 [70]. In contrast, no such shifts are observed in clusters containing heteronuclear diatomic molecules, such as CO. These differences in gas-to-cluster shift are assigned by using the quasiatomic approach [70]. The substantial blueshift of the N 1s → σ*-transition in nitrogen clusters can be rationalized in terms of dynamic core-hole localization and dynamic core-hole symmetry breaking in covalent molecular systems with equivalent atomic sites.

3.1.2.4. Hydrogen bonded clusters. Hydrogen bonded clusters are considerably stronger bound than van der Waals systems [1]. On the other hand, they are still weakly bound compared to covalent, metallic, or ionic systems. Water clusters represent a prototype system of hydrogen bonded species, which have been investigated by core level excitation near the O 1s-edge (530–545 eV) [78]. The near-edge absorption of variable size clusters was compared to that of molecular water [79]. The O 1s-absorption of water is characterized by three intense resonances that occur in the pre-edge regime, where both valence- and Rydberg-states are excited and there are two weak features corresponding to Rydberg states (see Fig. 9). The lowest energy resonance at 534.0 eV is due to the O 1s → $4a_1$-transition. It could also contain contributions from the $3sa_1$-Rydberg state. The other prominent features are found at 535.9 eV

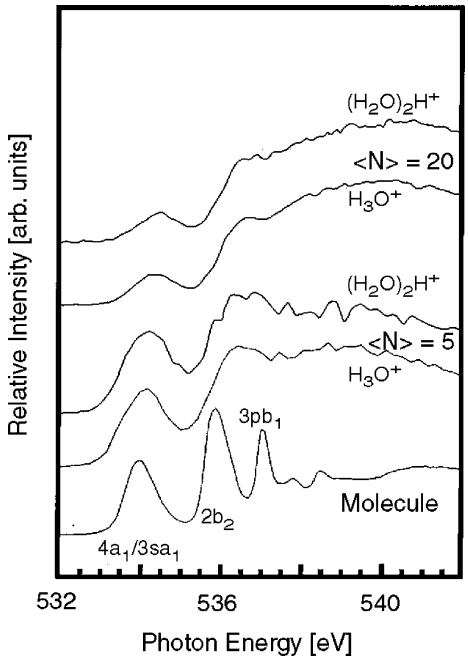

Fig. 9. Near-edge absorption of O 1s-excited molecular water (bottom trace) and water clusters of variable average cluster size $\langle N \rangle$. The data are adapted from [78].

(O 1s → $2b_2$-transition) and 537.1 eV (O 1s → 3p b_1-Rydberg-transition). The O 1s-absorption in free clusters has been investigated by photoion yields of mass-selected cluster fragments $(H_2O)_nH^+$, corresponding to pseudo-absorption spectroscopy [78]. Protonated clusters are stable products from ionic fragmentation of water clusters. These are known to be formed via proton transfer (see Section 3.5.3.2) [80]. Already the smallest cation that comes from clusters (H_3O^+) shows at $\langle N \rangle = 5$ an O 1s-absorption, which is quite different from that of the bare molecule [78]. The lowest energy resonance is broadened and slightly blueshifted, whereas the other ones have vanished in the intense continuous absorption. There is only a steep increase in the ion yield near 535.5 eV, which remains unstructured and flat above 536 eV. This situation is almost identical for larger cluster fragments as well as changes in $\langle N \rangle$ toward larger values, where a slight blueshift of the lowest energy resonance and an increase of the continuous absorption in the O 1s continuum is observed with increasing $\langle N \rangle$ [78]. The spectral blueshift is qualitatively interpreted, similar to earlier results on rare gas clusters [36], in terms a particle confined in a shrinking box [78] (see Section 3.3.1). As a result, the 'spatial restriction' of the final state valence orbital by the surrounding atoms in a cluster leads then to a blueshift. The broadening of the transitions in clusters were rationalized in terms of intermolecular vibrations and hybridization between neighboring molecules [78]. In addition, the coordination of the absorbing water molecule was considered in this work, where it was noted that the excitation energy increases with increasing coordination of water. This issue has been addressed in detail recently, where the O 1s excitation of liquid water and ice is discussed [81,82]. The O 1s-absorption of condensed water is quite similar to that of free microclusters. However, there are distinct differences between ice and liquid water, where the absorption of liquid water was measured by sampling the fluorescence [81]. We note, that more details on surface bound molecules and their local coordination environments in liquid water have been obtained from total electron- and total ion-yield measurements [82]. The intense pre-edge peak occurs in condensed water near 535 eV [81], i.e., at higher energy than in free clusters. This feature is considerably stronger in liquid water, and there are near 542 eV less distinct continuum resonances than in ice. X-ray absorption probes the local surroundings of the absorbing sites. Spectral simulations on condensed water, which are based on density functional theory [83] in combination with classical molecular dynamics calculations, have been reported earlier [84]. Three different local structures of hydrogen bonding are considered: (i) a symmetric H-bonded species, which is fully coordinated; (ii) an asymmetric network, where one bond is broken at the acceptor site, i.e., one oxygen lone-pair is not participating in a hydrogen bond; and (iii) an asymmetric network, that is asymmetric at a donor site, so that one hydrogen atom is not participating in hydrogen bonding [81]. The latter network is shown to give rise to the low lying resonance in the near-edge spectra of clusters as well as liquid and solid water. Consequently, an intense resonance in the pre-edge regime is proportional to the number of broken hydrogen bonds, so that the spectral evolution of the X-ray absorption in variable size water clusters reflects such changes [78]. One may conclude from the experimental results that the free clusters are most likely solid.

Finally, we note that other hydrogen bonded systems, such as methanol clusters, have been investigated before in the C 1s excitation regime [68]. Substantial changes in the near-edge are observed. These occur in the regime of lowest energy feature at 287.9 eV. This corresponds to the C 1s → 3sa′-Rydberg transition in the isolated molecule [79,85]. Rydberg transitions are sensitive to the local surroundings [86], so that these features are expected to undergo substantial broadening and spectral shifts in clusters, as outlined in Section 3.1.1.

3.1.2.5. Ionic clusters. Molecular clusters containing ionic species, such as sodium chloride, have been generated in a pickup source and were investigated in the Cl 2p- and the Na 1s-excitation regimes [87–91]. The near-edge structure was deduced from partial ion yields. It consists in the Cl 2p-regime of broad features that have been found for various fragment ions. These features were assigned by a comparison with simulated spectra that were obtained from multiple scattering calculations. Most interestingly, substantial size-dependent changes in bond length are anticipated to occur, according to model calculations [90,91]. These occur when the Na–Cl bond length is increased from $r_{Na–Cl} = 2.36$ Å

in the molecule [92] to $r_{Na–Cl} = 2.79$ Å in the solid [93]. The experimental results obtained in the Na 1s-excitation regime clearly indicate that there are characteristic changes in the ion yields as a function of cluster size [89,90]. These occur in the Na 1s-continuum as size-dependent changes in the X-ray absorption near-edge structure (XANES), which is due to multiple scattering processes. The assignment of the geometry changes is based on earlier work [94,95], yielding for $\langle N \rangle = 9$: $r_{Na–Cl} = 2.59 \pm 0.05$ Å and for $\langle N \rangle = 50$: $r_{Na–Cl} = 2.68 \pm 0.05$ Å [89,90]. The experimental results were compared to model calculations that consider the Coulomb interaction and the Born–Meyer repulsive interaction between ions inside the clusters [85,86], yielding good agreement with the experimental results.

More recent work concentrated on the geometry of the $(NaCl)_4$-cluster [88,91]. Three structures were considered in earlier work: (i) distorted cubes with T_d symmetry [96,97]; (ii) ring-shaped clusters [96]; and (iii) a ladder structure [97]. The experimental Na 1s- and Cl 2p-near-edge structure were used in comparison with multiple scattering calculations in order to derive the geometry of $(NaCl)_4$ [69]. Best agreement is obtained from both absorption edges with the distorted cube structure, which is in agreement with earlier theoretical work [96,97].

3.1.2.6. Covalent clusters. Free clusters of variable size containing covalently bound atoms can be produced by heating the corresponding solids. Recent examples for producing clusters by this simple approach are studies on variable size sulfur clusters, which were investigated near the K- and L-ledges [98–100]. Variable size clusters are obtained from evaporation of neat sulfur at different temperatures (375 K $\leq T \leq$ 565 K). As a result, the near-edge spectra show different shapes [99]. These are assigned to sulfur clusters of different sizes S_n, where $2 \leq n \leq 8$. Note that the formation of larger sulfur clusters requires adiabatic expansions of sulfur vapor [101].

The smallest cluster that is obtained from the simple cluster source, that relies on evaporation of sulfur, is S_2 [100]. It occurs with high intensity at $T > 500$ K. Its near-edge spectrum in the S 1s-regime is similar to that of O_2 near the O 1s-edge. Both species are similar in electronic structure, since they have an $X\ ^3\sum^-$ ground state [77]. The lowest unoccupied molecular orbital is the π^* orbital, corresponding to an intense, low lying resonance in the S 1s-excitation regime at 2469 eV. A hole in the K-shell produces $^4\sum^-$ and $^2\sum^-$ cation states. The exchange splitting in O_2 is known to be of the order of 1.1 eV in the ground state, it increases to ∼1.75 eV in the core-excited (O 1s → σ^*) molecule [102,103]. The exchange interaction in S_2 is smaller than in O_2, since the 1s orbital of sulfur is much deeper bound than the O 1s level. This result is in agreement with the experimental results (see Fig. 10) and ab initio calculations, where 0.75 and 1.15 eV are found, respectively [100]. Similar results were obtained from K-shell excitation studies on free selenium clusters, where an exchange splitting in Se_2 of 0.9 eV was reported [104]. This value was deduced from ab initio calculations, since it is not directly accessible in experiments due to considerable lifetime broadening in the Se 1s-regime ($E \approx 12.65$ keV). We note that the near-edge structure is somewhat less pronounced near the S 2p-edge, since spin-orbit splitting leads to substantial congestion of the near-edge features [105].

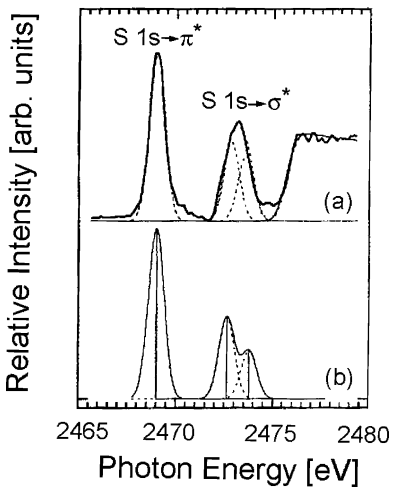

Fig. 10. Comparison of the experimental total cation yield spectra of S_2 with results from ab initio calculations: The experimental spectrum (thick line in (a)) is de-convoluted by Gaussian line shapes. The calculated spectrum (vertical lines in (b)) are broadened by these line shapes (see text and [100] for further details).

At reduced temperature of the oven source, i.e., at $T \approx$ 400 K one observes predominantly S_8 [98,106]. The S 1s excitation of S_8 contains more unoccupied states than can be reached by S 1s-excitation of S_2. These occur as a single, broad band that is centered at 2472 eV (see Fig. 11). Ab initio calculation indicate that most likely eight transitions

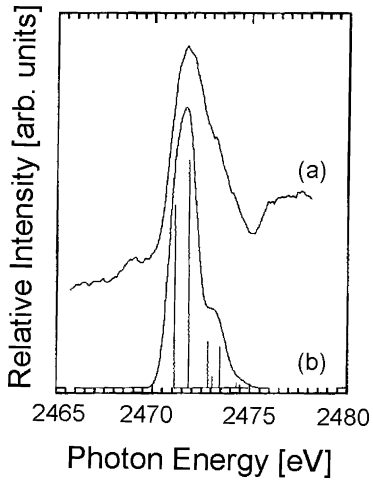

Fig. 11. Comparison of the experimental total cation yield spectra of S_8 (a) with results from ab initio calculations (b): The calculated spectrum (vertical lines in (b)) are broadened by Gaussian line shapes (see text and [100] for further details).

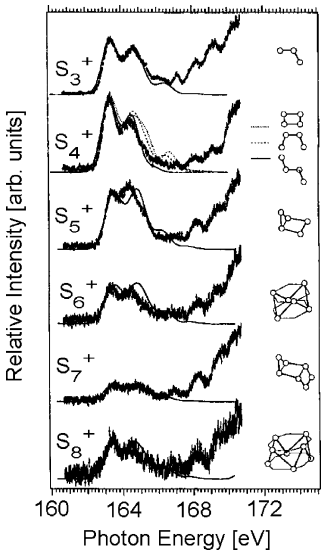

Fig. 12. Photoion yields of sulfur clusters (S_n^+, with $2 \leq n \leq 8$) recorded in the S 2p-excitation regime [99]. The spectra are simulated by using extended Hückel calculations (thin full and broken lines), where structural data from [108] were used.

contribute to this band [100]. Similar findings come from S 2p-excitation, where extended Hückel calculations were used to assign the electronic states which contribute to the lowest energy feature near 164 eV [98]. Moreover, this feature is broadened by spin-orbit splitting ($\Delta E \approx 1.2$ eV). It was investigated in greater detail, where photoion yields of mass-selected fragment ions were measured [99]. The experimental results indicate that there are distinct differences in shape, so that extended Hückel calculations, which make use of the equivalent ionic core virtual orbital model ('$Z+1$-approximation') [107], were applied in order to correlate the spectral shape of the 164 eV-band with the geometric structure of S_n-clusters ($3 \leq n \leq 8$) (see Fig. 12) [99]. Indeed, characteristic differences are found, which also give evidence that even different isomeric species can be distinguished from each other by near-edge absorption in the S 2p regime. For example, S_4 can occur in various isomers, where two cyclic and two open planar isomers (*cis*- and *trans*-isomers) were identified by earlier theoretical work [108–110]. Interestingly, earlier experiments using Raman spectroscopy found evidence for the occurrence of the *trans*-isomer [111], which is not the lowest energy isomer, according to theoretical work. Extended Hückel simulations of the lowest energy transition in the S 2p regime clearly indicate that best agreement with the experimental results is found for the *trans*-isomer. A substantially broader band is expected to occur in the case of the other isomers, so that their contributions to the experimental near-edge spectrum are discounted. The other sulfur clusters, that were investigated by the same approach, give in general good agreement between the experimental and simulated spectra, where the lowest energy isomers seem to be present in the gas phase.

Heterogeneous clusters containing sulfur have been investigated recently in the inner-shell absorption regime [112,113]. Variable size CdS clusters were prepared in a pickup source [112]. Their electronic structure was studied in the S 2p regime in comparison with CdS nanocrystals. The results indicate that there are significant differences in electronic structure between free clusters and deposited nanocrystals. A low-lying feature is observed at 162.7 eV, which was assigned as a Wannier-type excitonic feature in small CdS nanocrystals [114]. However, it is also possible that these transitions are due to low-lying unoccupied molecular orbitals, as discussed above for homogeneous sulfur clusters. Theoretical work addressed the importance of short-range electron-hole interactions in core-excited systems [115], so that excitonic absorption with respect to Wannier-type excitons is increased. As a result, the radius of the Wannier exciton is smaller in core-excited clusters than in valence band Wannier excitons. However, Nowak et al. concluded, that the similarity between the lowest energy transitions in free clusters and nanoparticles seems to be accidental [112], so that further experimental and theoretical studies in this field are proposed.

Heterogeneous transition metal sulfur clusters are known to occur in electron transfer proteins [116]. The electronic structure of free iron–sulfur clusters was investigated near the S 2p- and Fe 2p-, and Fe 3p-edges, giving rise to considerable chemical shifts in the near-edge structure, especially near the Fe-edges [113,117].

3.2. Geometric structure of free clusters

The lowest energy structures of free rare gas clusters are multishell icosahedra, where closed shells occur at [63]:

$$N = \tfrac{1}{3}(10\,s^3 - 15\,s^2 + 11\,s - 3), \quad (1)$$

where N is the total number of atoms in a cluster and s is the number of shells in a multishell icosahedron. The number of surface-bound atoms N_s is [63]:

$$N_s = 10\,s^2 - 20\,s + 12. \quad (2)$$

Closed icosahedral shells are expected for 13, 55, 147, 309, 561, 923, ... atoms. One may expect that the clusters grow further in five-fold symmetry, but it is known that the heavy condensed rare gases, such as Ne, Ar, Kr, and Xe, form a face-centered-cubic (fcc) lattice [3].

Earlier theoretical work predicts that the surface dominates the stability in small clusters, so that at least more than 10^4 atoms per cluster are required to form stable cuboctahedra [3], which have a higher binding energy than the corresponding icosahedra [65,118]. Experimental works suggest considerably lower cluster sizes for the occurrence of fcc-moieties. At least 750 [16] or 3500 [119] atoms per cluster are required to find evidence for fcc-structures. This discrepancy between the experimental and theoretical results motivated further investigations on the geometric structure of free, variable size argon clusters, where the

extended X-ray absorption fine structure (EXAFS) near the Ar 1s-excitation was measured and analyzed [39].

Extended X-ray absorption fine structure occurs as weak oscillations of the absorption or ionization cross section in core ionization continua. This approach is primarily sensitive to the nearest neighbor shell of the absorbing atom. Other shells that are collinear to the nearest neighbors can also be observed with high sensitivity by EXAFS, since there is a strong forward scattering component of the nearest neighbor shell [23,120]. In the case of the fcc-lattice of solid argon, the fourth shell is collinear with the nearest neighbor shell, which gives rise to two strong EXAFS-signals from these shells. In contrast, in the case of icosahedra one observes backscattering of the outgoing electron wave exclusively from the nearest neighbor shell. Therefore, EXAFS can be used as a sensitive probe for the occurrence of fcc-moieties in variable size rare gas clusters [39]. This was demonstrated by simulations of the EXAFS signal on 1s-excited argon clusters using the spherical wave approach (see Fig. 13) [121]. Two different geometries of variable size are considered: (i) fcc-structures and (ii) multishell icosahedra. Fig. 13 shows indeed that the simulated EXAFS-signal of variable size multishell icosahedra containing argon reflects exclusively the shell of nearest neighbors, since there are no other close lying shells collinear with the nearest neighbor shell.

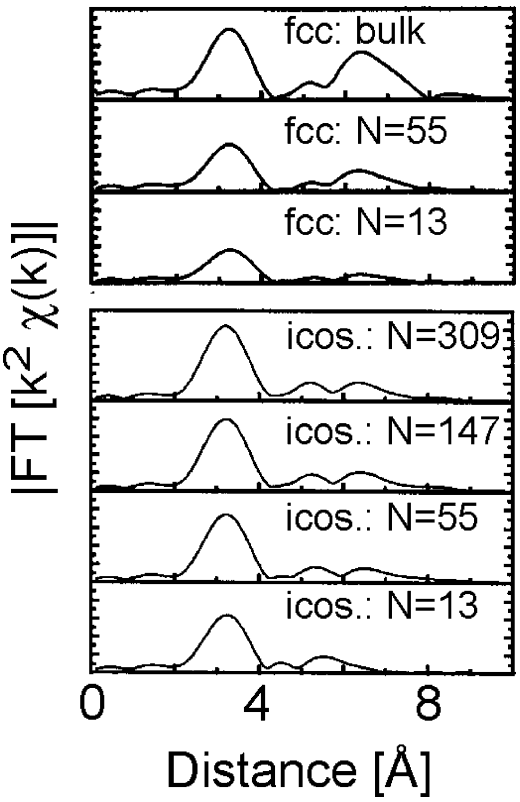

Fig. 13. Simulated mean radial distribution function $|\mathrm{FT}[k^2\chi(k)]|$, corresponding to the Fourier transform of the k^2-weighted EXAFS-signal, in variable size argon clusters Ar_N of fcc and icosahedral structure. The data were adapted from [39].

In the case of argon clusters one finds from the experimental EXAFS signal that the nearest neighbor distance is 3.76 Å [32,34,35,39], where the EXAFS in the Ar 2p-, Ar 2s-, and Ar 1s-continuum was analyzed. It is noted that the Ar 2p-EXAFS suffers from spin-orbit-splitting ($\Delta E \approx 2.15$ eV) and a fairly short energy range that can be analyzed because of the close lying Ar 2s-edge ($E \approx 325$ eV). This permits an EXAFS-analysis only from 250 to 310 eV, corresponding to the range $1 \leq k \leq 4$ of the photoelectron wave vector k. The Ar 2s-EXAFS has no such problems, but its analysis is difficult, since the Ar 2s cross section is quite weak and it is blended with the Ar 2p-EXAFS. Therefore, Ar 1s-EXAFS is the most obvious choice for investigations of the structural evolution of variable size argon clusters. However, the absorption cross-section of argon is fairly weak in this energy regime [122]. Therefore, first experiments using a dipole beam line suffered from weak signal intensity, so that no size effects in geometric structure could be observed [34]. Later attempts made use of an undulator beamline, where sufficient photon flux was available [39]. These results are discussed below in greater detail.

The Ar–Ar bond length is expected to be almost independent on the cluster size and shape. This follows from a comparison of the dimer [77] and the solid [123]. The only quantity that is expected to change is the number of nearest neighbors, which increases with cluster size, so that finally the bulk value of 12 is reached. The simulations, shown in Fig. 13, indicate that there is a second maximum in the EXAFS signal near ≈6.5 Å. This comes from the fcc-lattice and polycuboctahedra, which is clear evidence for scattering from the fourth shell [39]. The intensity of this maximum grows with increasing the number of fcc-sites near the absorbing atom. These findings are in agreement with the experimental EXAFS results.

The raw experimental spectra recorded in the Ar 1s excitation regime are shown in Fig. 14. They look quite similar to each other, but there are distinct differences in structural properties, if an EXAFS analysis is performed [39]. The fcc-sensitive second maximum in the EXAFS-signal near 6.5 Å

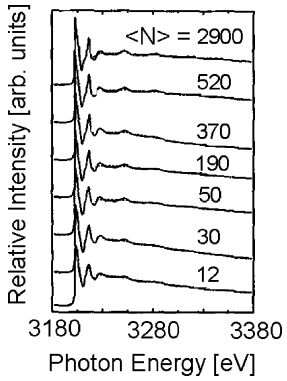

Fig. 14. Experimental cation yields of mass-selected fragments from variable size argon clusters in the Ar 1s-excitation regime [39]. The numbers indicate the average cluster size $\langle N \rangle$. The EXAFS signal corresponds to the weak oscillations of the cation signal above 3225 eV.

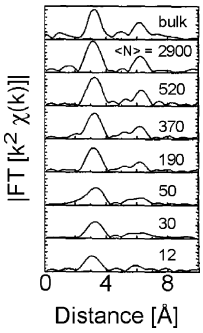

Fig. 15. Experimental mean radial distribution function $|\mathrm{FT}[k^2\chi(k)]|$ in variable size argon clusters, where the numbers correspond to the average cluster size $\langle N\rangle$. The bulk spectrum is adapted from [123]. Details on the data analysis can be found in [39].

radial distance occurs already with appreciable intensity at $\langle N\rangle \approx 200$, as shown in Fig. 15. The results obtained from EXAFS are rationalized as follows: the clusters are formed in the adiabatic nozzle expansion, where the supersaturated gas undergoes spontaneous nucleation by fast cluster growth. Perfectly shaped clusters with the lowest free energy are expected to grow slower than those containing defects, such as, e.g., stacking faults [124,125]. Theoretical work indicates that there is no evidence for a structural transition from icosahedra to fcc [126], rather than a persisting multiply twinned core of five-fold symmetry that is surrounded by a faulted shell with defects that stimulate the fcc-crystal growth. This growth mechanism also serves to prevent hcp-growth. Furthermore, these results are in agreement with earlier electron diffraction work [16], but evidently EXAFS is more sensitive to the occurrence of fcc-moieties in clusters. As a result, the size regime where fcc-structures are observed is lower than in previous experimental works.

EXAFS in free clusters has also been found in molecular van der Waals clusters containing benzene [68]. Photoion yields of mass selected cluster fragments and the bare molecule were used to distinguish between the intramolecular and the intermolecular EXAFS-signal in the C 1s excitation regime (280–380 eV). Fig. 16 shows the photoion yield of the dimer cation $(C_6H_6)_2^+$, where the intramolecular EXAFS is expected to give rise to a low frequency oscillation in the C 1s continuum (see Fig. 17). In contrast, the intermolecular EXAFS gives a higher frequency oscillation (see Fig. 17), since the EXAFS frequency is inversely proportional to the distance between the absorbing and backscattering site. In benzene clusters, predominantly backscattering from other carbon sites will contribute to the EXAFS signal, whereas contributions from the hydrogen sites are expected to be weak [23]. If one assumes that benzene clusters have a similar structure compared to solid benzene [127], then the absorbing site should have six nearest intermolecular neighbors at the same distance of ∼3.5 Å. This value is also in agreement with previous work on the benzene dimer, where an intermolecular C–C distance of 3.75 Å is expected to occur [128]. This value is similar to the result from the

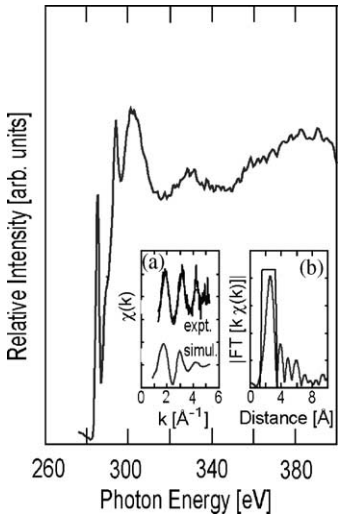

Fig. 16. Photoion yield of benzene clusters ($(C_6H_6)_2^+$ to $(C_6H_6)_8^+$) obtained from a benzene/argon expansion at $p_0 = 2.2$ bar and $T_0 = 300$ K. The insets correspond to: (a) experimental EXAFS signal and the back transformed EXAFS in comparison with the simulated EXAFS signal; (b) Fourier transform of the k^1-weighted EXAFS signal. See text and [68] for further details.

EXAFS-analysis (cf. Fig. 16), where the intermolecular C–C distance is found to be 3.45 Å [68]. Backscattering from other sites will appear with lower amplitude, so that it will not be easily detectable in the weak EXAFS-signal of benzene clusters. The experimental results indicate that there is evidence for a T-shaped geometry that occurs in free clusters, corresponding to the minimum of the potential energy surface [129]. We note that the structure of free benzene dimers was subject of discussion in the past, where different isomeric structures were identified, such as a parallel orientation of the rings, parallel displaced rings, and a T-shaped isomer [129–131]. Other isomers, such as a V-type structure, have also been discussed before [132]. It was pointed out in earlier theoretical work that most likely the potential energy surface of the benzene dimer ground state is shal-

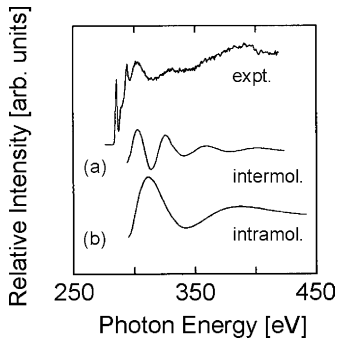

Fig. 17. Photoion yield of benzene clusters ($(C_6H_6)_2^+$ to $(C_6H_6)_8^+$) obtained from a benzene/argon expansion at $p_0 = 2.2$ bar and $T_0 = 300$ K (top) in comparison with the calculated intramolecular ($r_{C-C} = 1.41$ Å) (middle) and intermolecular EXAFS-signal (bottom). See text and [68] for further details.

low, so that several isomers may exist [133]. As a result, it may depend strongly on the spectroscopic approach, which of the isomeric structures are probed.

An example of size-dependent changes in free selenium clusters Se_n ($2 \leq n \leq 7$) has been presented recently [134]. It has been shown that photoelectron–photoion coincidence spectroscopy is suitable to obtain size-dependent structural information, where the coincidence signals of the highly charged atoms contain the size-sensitive information. By this approach it was possible to observe by EXAFS size effects of the Se–Se distance $r_{Se–Se}$, which changes from Se_2 ($r_{Se–Se} = 2.17(1)$ Å) to Se_n ($n \leq 5$: $r_{Se–Se} = 2.35(1)$ Å). These values are in good agreement with previous experimental and theoretical work on selenium clusters [77,135–137]. The advantage of the EXAFS approach is, that even small changes in bond length occur as significant changes in the frequency of the EXAFS signal.

We conclude that EXAFS spectroscopy is a sensitive probe to probe size effects in free atomic and molecular clusters, where the local geometry near the absorbing atom is investigated.

3.3. Inner-shell photoionization of free atomic and molecular clusters

Inner-shell photoionization of clusters gives detailed information on size effects of the occupied electronic shells and their dynamics. Core ionization energies of free atoms, molecules [17,19], and solids [138,139] have been investigated extensively in the past. However, size effects in inner-shell photoionization of free variable size clusters have only been investigated during the last decade, as will be outlined below. These experiments have the inherent advantage that they yield not only size effects in core ionization energies of clusters. Moreover they also serve as an independent way to determine core ionization energies of the condensed phase. This is of specific importance to samples that easily charge during the experiments, such as atomic and molecular van der Waals solids. Two different experimental approaches are commonly used: (i) excitation in an inner-shell continuum, where the kinetic energy of the photoelectrons is analyzed [36,46,47] and (ii) detection of low kinetic energy electrons, such as ZEKE photoelectrons [44,140], using the tunability of the radiation source. These approaches give complimentary results, as will be outlined in the following.

3.3.1. Excitation in inner-shell continua: X-ray photoelectron spectroscopy

Photoionization of variable size argon clusters at constant photon energy was reported for the first time by Björneholm et al. in the Ar 2p-excitation regime [36]. Later work included a detailed analysis of these results [55]. These works clearly indicate that the Ar 2p ionization energy drops from the atom to the bulk. This is a result of the polarization of the atoms that surround the ionized atom. Therefore, surface bound atoms show a smaller redshift of the Ar 2p-ionization energy than those atoms that are bound in the bulk. Specifically, the Ar $2p_{3/2}$ ionization energy shifts as a function of cluster size for surface bound atoms from the atom ($IE(Ar\,2p_{3/2}) = 248.63$ eV [141]) to ∼247.95 eV in small clusters and ∼247.75 eV in large clusters. The bulk ionization energy is found near ∼247.6 eV. From classical polarization screening models one obtains a $N^{-1/3}$ dependence [1,142]. This was used by Björneholm et al. in order to extrapolate the Ar $2p_{3/2}$ ionization energy of solid argon, where $\langle N\rangle^{-1/3}$ was plotted as a function of the experimental results from photoelectron spectroscopy (see Fig. 18). In addition, the size-dependent transition energies into the lowest Rydberg-/exciton-state are included in the lower part of Fig. 18 [36]. This gives a redshift of the Ar 2p ionization energy of bulk sites relative to the atomic value of -1.0 ± 0.05 eV. This value is considerably more reliable compared to earlier work on condensed argon [57,143,144], where energy shifts between −2.4 eV [57] and +0.1 eV [144] are reported. Further details can be found in [36]. Moreover, the binding energy difference between surface and bulk sites in solid argon is 0.3 eV (see Fig. 18). These results were also used to derive an effective coordination number of surface bound atoms in variable size clusters [36]. This quantity varies from 5.3 in small clusters ($\langle N\rangle \approx 10$) to 7.8 in large clusters ($\langle N\rangle \approx 4000$). These values are expectedly substantially smaller than the coordination number of bulk atoms in fcc-solids, where a value of 12 occurs.

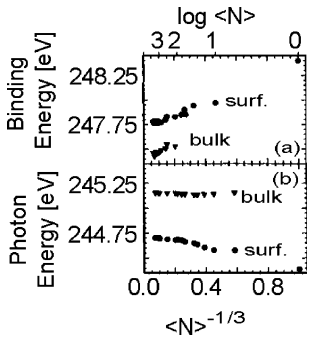

Fig. 18. (a) Experimental Ar $2p_{3/2}$ binding energy as a function of the average cluster size $\langle N\rangle^{-1/3}$, where surface and bulk components are clearly separated from each other; (b) experimental Ar $2p_{3/2} \rightarrow$ 4s-transition in variable size argon clusters. The transition is also split as a result of different excitation energies for surface and bulk sites. The data are adapted from [36].

Molecular clusters, such as $(H_2O)_n$, have been investigated by the same experimental approach [78]. A decrease in O 1s binding energy of 1.1 eV was found for small clusters, it increases to 1.3 eV in large clusters. However, it was not possible in this work to distinguish O 1s ionization from surface and bulk sites. This is mostly a result of substantial line broadening in the photoelectron spectrum. The decrease in core level binding energy was also assigned in terms of polarization screening, since it was assumed that intermolecular hybridization is not efficient in hydrogen bonded clusters [78].

3.3.2. Excitation near absorption edges: zero kinetic photoelectron spectroscopy

The use of a tunable radiation source in combination with the detection of ZEKE photoelectrons [145,146] gives comparable results to XPS [140]. The advantage of using the tunability of the radiation source is, that additional information on the dynamics of the inner-shell photoionization process can be obtained. The core hole is filled by an outer-shell electron, so that in the case of light elements an Auger electron is emitted. If this process is investigated near the core ionization threshold, then the fast Auger electron can overtake the slow photoelectron. In this case, it becomes possible that the photoelectron cannot be emitted into the vacuum, it is rather retained by the ionic system. This energy transfer process from the photoelectron to the Auger electron is commonly called post-collision interaction (PCI) [147–154], it shifts the ZEKE peaks to higher photon energy compared to the binding energy that is obtained from photoelectron spectroscopy. Note that PCI also affects resonant Auger spectra of atoms [155] and clusters [47], as will be outlined below (see Section 3.4.1). The ZEKE signal shapes are asymmetric, as a result of the PCI life time [151]. They may also be broadened, which corresponds to a Gaussian line shape. Spectral de-convolutions of the experimental ZEKE signals give the same core ionization energies as XPS, but in addition the PCI life time can be derived from spectral de-convolutions (cf. [151]). In addition, the absolute energy scale is quite accurately determined in ZEKE experiments, since the transition energies of Rydberg- and core-to-valence-transitions are well-known. These excitations give also rise to low kinetic energy photoelectrons, which are observed in ZEKE spectra as symmetric lines.

First ZEKE experiments on core-excited clusters yielded a gas-to-solid shift of the Ar $2p_{3/2}$ ionization energy of 1.0 ± 0.1 eV [140], which is in full agreement with XPS results (see above) [36]. ZEKE spectra also give specific information on the inelastic scattering of photoelectrons in the bulk interior of the clusters. These occur in the Ar 2p-continuum with strong intensity [140]. This follows from experiments where the same value of $\langle N \rangle$ was obtained from different expansion conditions, but in one case the background pressure was considerably reduced. Identical ZEKE spectra were found in both cases, which leads to the conclusion, that the inelastic scattering occurs within the clusters rather than in the gas phase around the photoionized cluster. The sensitivity of ZEKE electrons to bulk properties also occurs in the dominant signal of bulk excitons (e.g., in the Ar $2p_{3/2} \rightarrow$ 4s-regime) in a $\langle N \rangle$-regime that still shows in total electron yields considerable contributions of surface excitons [140]. First ZEKE experiments were performed with low spectral resolution [140], which did not permit a detailed analysis on changes in inner-shell photoionization dynamics. PCI profiles of surface and bulk sites require high resolution experiments, which have become available recently. A detailed analysis of recent results will be given elsewhere [156].

Finally, we note that ZEKE spectroscopy has been applied to study shifts of core level photoionization of molecular clusters as well as heterogeneous clusters containing variable amounts of atoms and molecules [44]. In the case of the N 1s ionization energy of nitrogen and its clusters one observes a redshift of 0.6 eV compared to the isolated molecule (IE(N 1s) = 409.9 eV [44]). This shift already occurs in small clusters, so that it is most likely due to surface bound molecules. This result is also in agreement with recent high resolution ZEKE work [156] as well as photoionization studies on condensed nitrogen, where a substantially lower N 1s ionization energy of 408.85 ± 0.15 eV has been reported [157].

3.3.3. Core level satellites

Photoelectron spectroscopy does not only serve for the identification of core ionization energies. More recently the satellite structure of free, variable size rare gas clusters containing neon and argon has been investigated [45]. The results were compared to earlier work on atomic and solid rare gases [158,159]. The following changes occur upon cluster formation: (i) the occurrence of a step-like structure, which corresponds to the onset of interband transitions. This region extends to low kinetic energy electrons and increases in intensity with decreasing kinetic energy, where inelastic losses dominate; (ii) a shift of the main lines by 0.5 eV to lower binding energy. This is due to a redshift in ionization energy as a result of polarization screening [46]; and (iii) new features occur as a result of the excitation of excitons. The latter features can also be found in energy loss spectra of the corresponding solids. In photoelectron spectra of clusters such processes occur as satellite lines resulting from energy losses of the outgoing photoelectron due to exciton formation inside the cluster.

3.4. Relaxation of core-excited clusters

The core hole is filled by electrons from outer electronic shells. This electronic relaxation leads to the emission of Auger electrons in the case of light elements, whereas the emission of X-ray photons dominates for heavy elements [18]. Relaxation processes in free clusters have been investigated by Auger electron spectroscopy and yields of Auger electrons. To the best of our knowledge, there are to date no experiments on the X-ray emission on weakly bound clusters in the gas phase. However, the emission of low energy photons may occur, if the relaxation process produces excited species, which relax via the emission of fluorescence photons. The following sections highlight recent results on van der Waals clusters with respect to electronic relaxation and the emission of low energy photons in the ultraviolet and vacuum-ultraviolet regime.

3.4.1. Electronic relaxation

Fig. 19 shows Auger electron yield (AEY) spectra, which are recorded at different average cluster sizes $\langle N \rangle$,

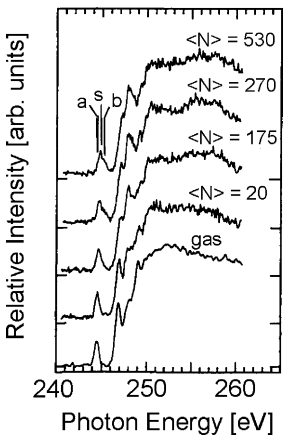

Fig. 19. Auger electron yield spectra of variable size argon clusters in the Ar 2p regime [160]. The labels near the lowest energy resonance (Ar $2p_{3/2} \rightarrow$ 4s-transition) are: a: atom; s: surface; b: bulk. See text for further details.

where electrons of ≈200 eV kinetic energy are selected [160]. The atomic spectrum, corresponding to the bottom trace in Fig. 19, is similar in shape to the total electron yield spectrum [32]. Discrete resonances are found in the near-edge regime at 244.4 and 246.9 eV, corresponding to resonant excitations into Rydberg states $Ar(2p_{3/2}) \rightarrow 4s$ and $Ar(2p_{3/2}) \rightarrow 3d$, respectively. In addition, there is high intensity in the Ar 2p-continuum, where the direct LMM-Auger process dominates. As the average cluster size is increased, the following changes are observed: (i) the $Ar(2p_{3/2}) \rightarrow 4s$ signal evolves as a complex shape with an increase in average energy, similar to total electron yields (cf. [32,53]); (ii) a broad $Ar(2p_{3/2}) \rightarrow 3d$ exciton line builds in at 247.8 eV, whereas the atomic Rydberg transition at 246.9 eV decreases in intensity; and (iii) weak oscillations appear in the Ar2p-continuum, which come from Ar 2p-EXAFS (cf. [32]).

Total electron and cation yield spectra of variable size argon clusters indicate that surface and bulk excitons can be identified by their energy positions [32,36,53]. There is a small blueshift of ≈0.35 eV for surface excitons, whereas bulk excitons are blueshifted by ≈1 eV [32,36], similar to solid argon [58]. The maximum of the lowest exciton state at 244.8 eV shows a shift in the case of large clusters ($\langle N \rangle = 530$), which is typical for surface excitons, contrary to TEYs [32] and ZEKE photoelectron yield spectra [44,140] recorded at identical expansion conditions. In the latter spectra a more intense contribution of the bulk transition is observed [32]. Another difference concerns the intensity of EXAFS oscillations in the Ar 2p-continuum. The first maximum at 256 eV is weaker in intensity in AEY spectra as compared to earlier TEY experiments [32]. The differences between the AEY and TEY in the Ar 2p-continuum are another indication of the surface sensitivity of the Auger electron yields [160], which show some similarity to the Auger yield of condensed argon [161]. However, some deviations occur in the regime of the lowest exciton which is still more intense and less blueshifted for clusters (244.8 eV) than for multilayers of condensed argon (245.1 eV). These differences between AEY spectra of free clusters and adsorbed argon are likely related to the dominant contribution of the surface in clusters. The smaller blueshift of the 4s-exciton, compared to the multilayer spectrum, may therefore be an indication that primarily surface atoms contribute to the Auger yield of microclusters, even though the penetration depth of 200 eV electrons is expected to be at least of the order of 3–4 atomic layers.

More recently, resonant Auger spectra of free clusters have been measured [46,47]. The photon energy was set to the atomic, surface, and bulk value of the Ar $2p_{3/2} \rightarrow$ 4s-transition [46]. The resonant Auger spectrum of the atom is well-known from earlier work [162,163]. The corresponding features in clusters are redshifted by 0.48 eV for surface sites and 0.62 eV for bulk sites, as evidenced from the $(2p^{-2})3d\ ^2D_{3/2}$ peak at 33.6 eV binding energy [46]. This shift is considerably smaller than for the single hole states, where energy shifts of 0.63 and 0.91 eV were found, respectively [36]. It is believed that polarization screening also accounts for the redshift in resonant Auger spectra. However, in two-hole one-particles states, where, e.g., a 3d-orbital is populated in the resonant Auger process, the spatial confinement of the excited electron by the surroundings in a cluster changes the situation compared to photoionization [36]. This explains qualitatively the smaller redshift in resonant Auger spectra [46].

Partial electron yields of selected Auger channels of variable size argon clusters have been reported recently [47]. This approach permits the selection of atomic and clustered species. As a result, it is possible to identify selectively Rydberg- and exciton-states in the 2p-continuum that are blended in the absorption and ionization cross section. In addition, resonant Auger spectra of clusters that are recorded on the surface and bulk $2p_{3/2}{}^{-1}3d$-resonances (surface: 247.5 eV; bulk: 247.9 eV) show substantial broadening as a result of PCI [47].

3.4.2. Radiative relaxation

Core-excited clusters may undergo radiative relaxation, if electronically excited species are formed. The emission of fluorescence photons may either occur in the soft-X-ray regime or at considerably longer wavelengths, i.e., in the ultraviolet or vacuum ultraviolet regime. The emission of low energy photons has been extensively studied in free van der Waals clusters for the outer-shell excitation regime (see, e.g. [29,164,165]). There is considerably less information on radiative relaxation processes of core-excited van der Waals clusters.

The occurrence of fluorescence from a broad continuum (165 nm $\leq \lambda \leq$ 290 nm) has been reported for Ar 2p-excited argon clusters [50] (see Fig. 20). This fluorescence channel is exclusively found in the Ar 2p-continuum, which is unlike the fluorescence behavior of atomic 2p-excited argon [50,166,167]: Fluorescence in the UV and visible regime

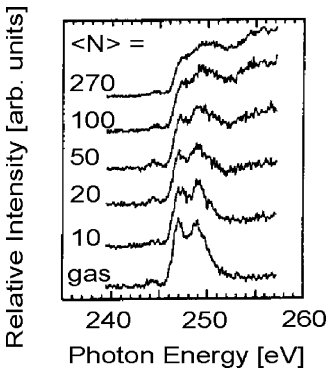

Fig. 20. Fluorescence excitation spectra of atomic argon (bottom) and variable size argon clusters at different average cluster sizes ⟨N⟩. See text and [50] for further details.

occurs with appreciable intensity in a narrow energy regime near the Ar 2p-edge (see Fig. 20). This channel is due to the fluorescence of the singly charged atom Ar^+, which is formed with low cross section in the Ar 2p-continuum. As a result, the fluorescence excitation spectrum of the atom is similar in shape compared to the Ar^+-yield [50,153,166], where mostly low lying Rydberg states contribute to the fluorescence yield near the Ar 2p-edge. As soon as clusters are present in the jet, one observes short wavelength fluorescence in the Ar 2p-continuum. Note that no discrete features are found in the fluorescence excitation spectrum (see Fig. 20 and [50]).

These findings are assigned in terms of the occurrence of the 'third continuum' of argon, which was found by various other experimental approaches, where argon was investigated at considerably higher pressure by ionizing radiation, particles, or in plasmas [168–170]. The assignment of this continuum radiation is based on models that have been developed by Langhoff, who suggested that doubly charged dimers, i.e., Ar_2^{++}, contribute to this radiative relaxation channel [171,172]. This assignment appears to be quite reasonable, since double ionization dominates in the Ar 2p-continuum, whereas below the Ar 2p-edge single ionization is dominant [173]. Moreover, the emission of continuous radiation is expected to occur from relaxation of Ar_2^{++}, since this dication decays via a bound-to-free transition into 2 Ar^+, as evidenced from Rittner potentials [171,172]. This mechanism offers one possibility to rationalize charge separation in core-excited clusters. This issue is discussed in greater detail in Section 3.6 along with other models.

3.5. Fragmentation of core-excited clusters

3.5.1. Doubly charged atomic clusters

Fragmentation of core-excited clusters becomes already evident from mass spectra, where the mass distribution is concentrated at much smaller masses than estimated from the average cluster size ⟨N⟩ [32]. As a result, photoion yields of mass-selected, light, singly charged fragments from van der Waals clusters, such as dimers and trimers, reflect changes in electronic structure as a function of ⟨N⟩ (see Table 1 and Section 2). However, mass spectra give no direct information on the fragmentation mechanisms of singly, doubly, and multiply charged clusters [3].

Fragmentation mechanisms of free molecules have been obtained from coincidence experiments [51,174], such as PIPICO, PEPIPICO, or PEPIPIPICO.

We discuss in the following results that have been obtained from experiments on core-excited rare gas clusters [31,43,44,68,160]. Fig. 21 shows a PIPICO spectrum of Ar 2p-excited argon clusters, where correlated cation pairs are observed [31], if clusters are present in the jet. In the case of argon clusters one observes three series of cation pairs, where the lighter moiety is either Ar^+, Ar_2^+, or Ar_3^+, corresponding to asymmetric fission (see Fig. 21). Information on symmetric fission processes, where cation pairs of the same mass are formed, occur as a blended signal at $\Delta t = 0$ in PIPICO spectra, where only time-of-flight differences between correlated cations are detected. The PIPICO signals have a considerable width, which is a result of the substantial kinetic energy release that comes from fission of doubly charged clusters. It is often assumed that electrostatic repulsion of the positive charges is the major source of the kinetic energy release. Therefore, charge separation distances can be deduced from simple electrostatic model considerations [42,51]. In addition, the experimental results yield plausible fission mechanisms. However, it turns out in the case of clusters, which are formed in wide size distributions, that there is some ambiguity in the assignment to a unique fission mechanism using PIPICO spectra [31]. In contrast, photoelectron–photoion–photoion-coincidence experiments give detailed information on the fission mechanisms of doubly charged molecular clusters [43]. Fig. 22 shows the three dimensional shape of the PEPIPICO spectrum of Ar 2p-excited argon clusters at $\langle N \rangle = 60$ ($E = 260$ eV), where the flight times of correlated cation pairs and their correspond-

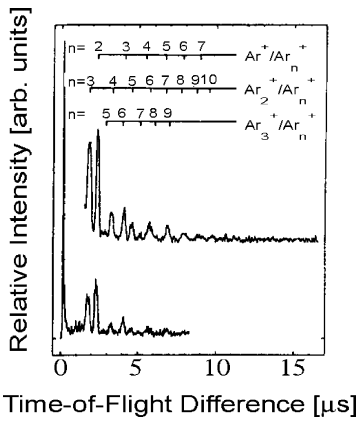

Fig. 21. Photoion–photoion coincidence (PIPICO) spectrum of argon clusters. Experimental conditions: $\langle N \rangle \approx 40$, excitation energy: 248 eV. The top spectrum corresponds to a vertically enlarged view of the bottom spectrum in order to show coincidence signals at large time-of-flight differences [31].

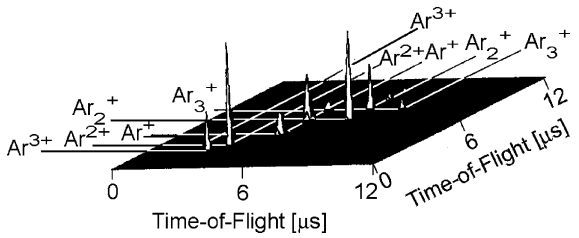

Fig. 22. Photoelectron–photoion–photoion coincidence (PEPIPICO) spectrum of argon clusters. Experimental conditions: $\langle N\rangle \approx 60$, excitation energy: 260 eV [43]. The lines are inserted in order to guide the eye.

ing intensity are plotted. The correlated cation pairs result in the Ar 2p continuum primarily from fission of doubly charged clusters (cf. Figs. 22 and 23). Two different fission processes are observed: (i) symmetric fission and (ii) asymmetric fission. Along the main diagonal, where the flight times of both cations are identical, one observes symmetric fission, corresponding to correlated cations of the same mass-to-charge ratio. These processes cannot be resolved by PIPICO as mentioned above (cf. [31]). The following cation pairs are observed, which come from symmetric fission: Ar^+/Ar^+, $Ar_2{}^+/Ar_2{}^+$, and $Ar_3{}^+/Ar_3{}^+$. There are no larger symmetric fission products, even though at $\langle N\rangle = 60$ considerably larger neutral clusters are present in the jet. At low $\langle N\rangle$ primarily symmetric fission is observed. However, the relative intensity of the symmetric channels decreases with increasing $\langle N\rangle$ [43], so that increasing intensity of the asymmetric charge separations is found off the main diagonal [43]. These cation pair series consist of a light cation that is correlated with a heavier one, similar to PIPICO spectra (cf. Fig. 21): $Ar^+/Ar_n{}^+$, $Ar_2{}^+/Ar_n{}^+$, and $Ar_3{}^+/Ar_n{}^+$, with $n \leq 12$. Insight into the fission mechanisms is obtained from the peak shape and slope analysis of the coincidence signals [43,51]. The PEPIPICO signals are found to change their shape and slope with increasing $\langle N\rangle$. This is clear evidence for size-dependent fission mechanisms, which occur for each PEPIPICO signal [43]. Fig. 23 shows, as one typical example, the evolution of the $Ar^+/Ar_2{}^+$-coincidence signal as a function of $\langle N\rangle$. The occurrence of this cation pair requires a neutral precursor of a least three atoms (Ar_n, $n \geq 3$). Photoionization and subsequent relaxation of the core hole likely forms an intermediate $Ar_n{}^{++}$, with $n \geq 3$. This dication may decay into the observed cation pair

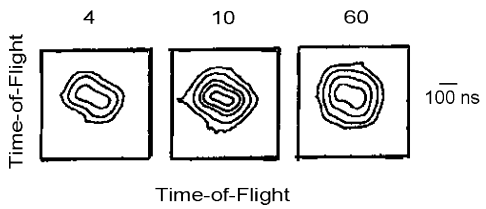

Fig. 23. Contour plots of the $Ar^+/Ar_2{}^+$ coincidence signal at different average cluster sizes $\langle N\rangle$, as indicated above the contour plots. The results are obtained from photoelectron–photoion–photoion coincidence (PEPIPICO) spectra of argon clusters [43].

$Ar^+ + Ar_2{}^+$, evaporating an unknown quantity of neutral atoms either before or after fission. The minimum dication size ($Ar_3{}^{++}$) involves a two body dication decay, corresponding to a slope of the PEPIPICO-signal of -1, which follows from the conservation of linear momentum [51]. In contrast to this, one finds for the cation pair $Ar^+/Ar_2{}^+$ at the threshold of cluster formation ($\langle N\rangle = 4$) that the experimental slope is -0.66 ± 0.04. Therefore, this cation pair cannot be formed by a simple two body decay rather than by a more complicated mechanism. A signal slope smaller than -1 involves the loss of one or more neutral atoms from the heavier moiety *after* the fission step. In contrast, a loss of neutrals prior to fission would give the same slope as for the two body decay, i.e., one expects also a slope of -1 for such process [51].

The experimental PEPIPICO-signal slope that is observed for the $Ar^+/Ar_2{}^+$-channel at $\langle N\rangle \approx 4$, corresponding to the threshold of the cation pair, is rationalized by the following fission mechanism:

$$Ar_4{}^{++} \rightarrow Ar^+ + Ar_3{}^+ \quad (3)$$

$$Ar_3{}^+ \rightarrow Ar_2{}^+ + Ar \quad (4)$$

Note that the mass ratio of the cations that are involved in the second step (cf. Eq. (4) and [51]) determines the experimental slope of $-2/3$. At this point it is not clear, whether the cluster dications are already smaller in size than the neutral precursors. Such evaporation of neutrals prior to fission cannot be investigated by PEPIPICO spectroscopy. However, the size-dependent shape of the $Ar^+/Ar_2{}^+$-PEPIPICO signal, shown in Fig. 23, is a clear indication for losses of neutrals after fission. An increase of the average cluster size to $\langle N\rangle = 10$ yields a twisted signal, where the main slope is increased to ≈ -0.35 (cf. Fig. 23, middle). This slope is rationalized using the same mechanism, as outlined in Eqs. (3) and (4), but starting from a larger neutral cluster, where more neutrals are evaporated in the second step that follows primary fission:

$$Ar_7{}^{++} \rightarrow Ar^+ + Ar_6{}^+ \quad (5)$$

$$Ar_6{}^+ \rightarrow Ar_2{}^+ + 4Ar \quad (6)$$

A further increase to $\langle N\rangle = 60$ gives a round-shaped coincidence signal (cf. Fig. 23, right hand side), where it is impossible to derive a meaningful signal slope. This signal is thought to be due to fission, where most likely the momenta of both singly charged fragments are not directed into opposite direction. As a result, one can assume that the simple picture of Coulomb explosion is not any more applicable to the size regime that is close to the critical stability N_{crit}, where two charges can be accommodated without immediate fission. It is known that this stability limit corresponds in the case of doubly charged argon clusters to N_{crit} (Ar) = 91 [175]. Thus, the singly charged fragments may be ejected at arbitrary angles which is reflected by the round shape of the $Ar^+/Ar_2{}^+$-coincidence signal [43].

3.5.2. Fission of triply charged atomic clusters

Dissociative triple ionization leads to singly charged fragments. These are unequivocally identified by multi-coincidence experiments, such as PEPIPIPICO [160]. This method has been applied earlier for investigations on isolated molecules undergoing multiple ionization [174,176].

The presentation of PEPIPIPICO signals requires, in principle, a four-dimensional plot, unless one uses projections. One simple approach to show such results is to sum the flight times of two correlated cations and plot them together with the flight time of the third cation, where the intensity of the coincidence signal corresponds to the vertical axis. As a result, three-dimensional plots are obtained, similar to PEPIPICO spectra (see Fig. 24).

Size effects in fission of triply charged argon clusters are shown in Fig. 24, where a series of PEPIPIPICO spectra is depicted, which were recorded at $\langle N \rangle = 10$, 20, and 175, respectively. This size regime is well below the critical size of stable triply charged argon clusters, which are known to require more than 226 atoms [177]. Fig. 24 (top spectrum) has been recorded at $\langle N \rangle = 10$, where a weak signal $Ar^+/Ar^+/Ar^+$-signal occurs. This implies that small triply charged argon cluster decay preferably into singly charged atoms as well as a given number of unseen neutrals that are lost by evaporation. This may happen most likely after fission.

With increasing $\langle N \rangle$ one observes that not only singly charged atoms are formed via fission, but also correlated dimer cations [160]. At $\langle N \rangle = 175$ the $Ar_2^+/Ar_2^+/Ar_2^+$-signal is the most intense fission channel (cf. Fig. 24, bottom spectrum). This finding agrees with results on dissociative double ionization of argon clusters, where the dimer cation is found to be the dominant species that is involved in fission [43]. The mechanism for the formation of dimer cations in fragmentation following dissociative triple ionization can be rationalized in analogy to dissociative double ionization: Fission of triply charged clusters leads to the primary ejection of singly charged atoms or dimers leaving a doubly charged cluster cation behind, which is subsequently stabilized by a second fission step. Moreover, simultaneous fission into singly charged cations may also occur. We note that a detailed slope analysis of these processes has not been reported yet, so that it is not clear whether sequential or simultaneous fission processes occur. More recent work on multiple ionization of argon clusters induced by collisions with multiply charged ions indicates that even correlated, multiply charged atoms are formed [178]. Such products have not been observed in experiments relying on one-photon absorption, even in the hard X-ray regime, e.g., near the Ar 1s-excitation ($E \approx 3.2$ keV) [34]. These differences in charge state of the final products are rationalized as follows: the processes leading to multiple ionization originate in inner-shell excitation from the site that absorbs the photon. As a result, the excited center or its near surroundings contain initially the positive charges, which may delocalize prior to fission. In contrast, collisions with highly charged ions remove several outer-shell electrons in a short time scale, which is of the order of a few femtoseconds [178]. Charge localization, which has been quantified by a Coulomb overbarrier model [179], leads to high charge states of individual atoms in argon clusters. As a result, multiply charged atoms are observed after fission. This is different from metal clusters and fullerenes [180–186], where a higher charge mobility leads mostly to singly charged fragments.

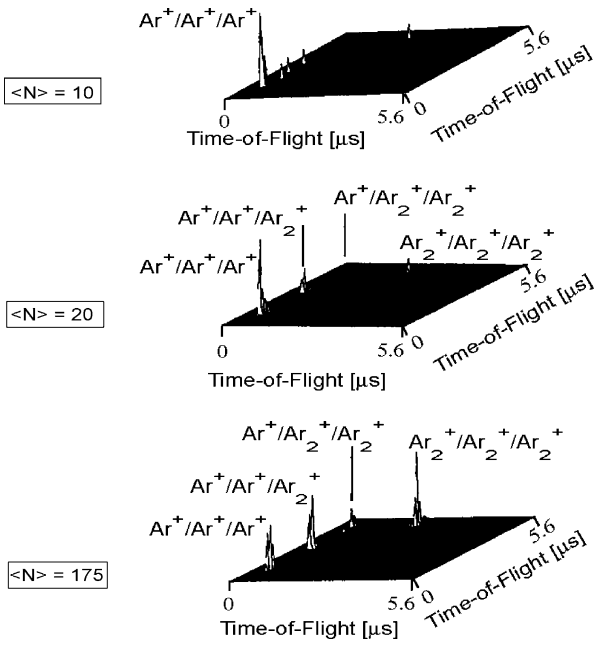

Fig. 24. Photoelectron–photoion–photoion–photoion coincidence (PEPIPIPICO) spectra of argon clusters recorded at different average cluster sizes $\langle N \rangle$. The spectra correspond to a projection of the raw data, where one flight time is plotted vs. the sum of the flight times of the other two correlated fragment ions. The intensity of the coincidence signals is plotted on the vertical scale (see text and [160] for further details).

3.5.3. Fission of core-excited molecular clusters

3.5.3.1. Nitrogen clusters. Charge separation of nitrogen clusters has been reported earlier using PIPICO [67] and PEPIPICO spectroscopy [44]. The critical size of stable doubly charged nitrogen clusters is $(N_2)_{99}^{++}$ [187]. Four series of fission channels are identified: (i) $N^+/(N_2)_n^+$; (ii) $N_2^+/(N_2)_n^+$; (iii) $(N_2)_2^+/(N_2)_n^+$; and (iv) $N_3^+/(N_2)_n^+$ (see Fig. 25(a)). Symmetric charge separation, which is found along the main diagonal, is considerably weaker than the asymmetric channels. This is unlike results on argon clusters (cf. Fig. 22 and [43]).

The shape of the $N_2^+/(N_2)_n^+$-PEPIPICO signal is shown in some more detail (see Fig. 25(b) and (c)). Two different expansion conditions are compared in these figures in order to investigate the dependence of the peak shape on the average cluster size $\langle N \rangle$ of the neutral clusters. The contour plot shown in Fig. 25(b) has been recorded in the threshold regime of cluster formation, where the beam is composed mostly of small clusters, corresponding to $\langle N \rangle \approx 10$ (cf.

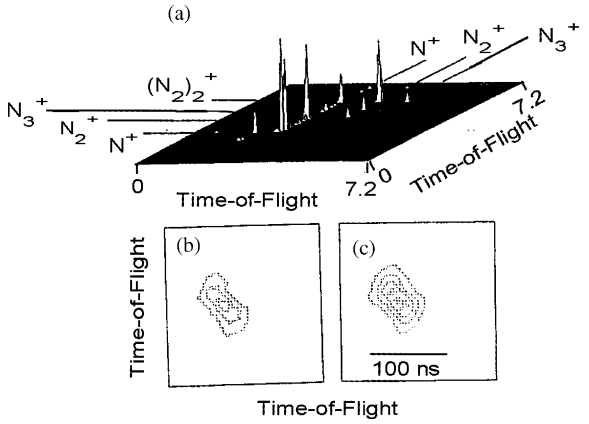

Fig. 25. (a) Photoelectron–photoion–photoion coincidence (PEPIPICO) spectrum of nitrogen clusters ($\langle N\rangle \approx 150$); (b) contour plot of the $N_2^+/(N_2)_2^+$ coincidence signal at the threshold of cluster formation ($\langle N\rangle \approx 5$); (c) contour plot of the $N_2^+/(N_2)_2^+$ coincidence signal at $\langle N\rangle \approx 150$ [44].

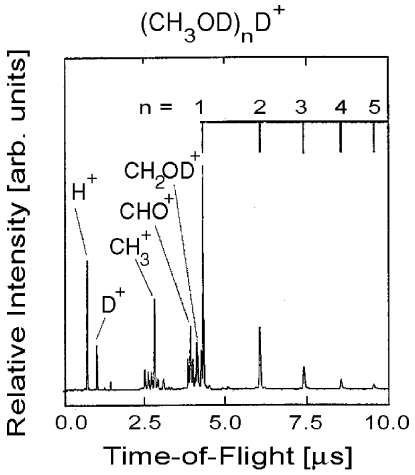

Fig. 27. Photoelectron–photoion coincidence (PEPICO) spectrum of *o*-deuteromethanol clusters. Experimental conditions: $E = 289$ eV; $T_0 = 300$ K; $p_0 = 2.4$ bar, seed gas: He [188].

[28]). The photoionization mass spectrum shows at these conditions mass lines up to $(N_2)_9^+$. The peak shape shown in Fig. 25(c) corresponds to $\langle N\rangle \approx 150$, where the mass spectrum contains cluster ions up to $(N_2)_{30}^+$. The shapes of both coincidence signals are similar to each other, also the slope is in both cases close to -1, but the signal strength has increased if larger clusters are present in the jet. This implies that the $N_2^+/(N_2)_2^+$-pair is most likely formed via a deferred charge separation mechanism (cf. [51]). Primarily evaporation of neutrals shrinks the cluster dication. Subsequent fission leads to the singly charged products. We note that this charge separation mechanism is different from the findings on rare gas clusters (see Section 3.5.1).

3.5.3.2. Methanol clusters. Fission of methanol clusters has been investigated recently, as an example of a cluster system that consists of polyatomic molecules that can undergo various intramolecular and intermolecular fragmentation mechanisms [42,188].

Fig. 26 shows an overview PEPIPICO spectrum of C 1s-excited *o*-deuteromethanol (CH_3OD) ($E = 289$ eV). The isotope-labeled compound has been chosen in order to distinguish the hydrogen sites at the methyl group from that at the oxygen site. It is well-known from earlier work on outer shell photoionization, leading to singly charged methanol clusters, that protonated fragment ions are formed [189,190]. Proton transfer from the hydroxyl group is the origin of the atom that contributes to protonated fragments. In contrast, the methyl group plays a minor role in this fragmentation mechanism [188]. The present experimental results clearly show that fission yields the same final products as observed in single ionization, i.e., in the case of *o*-deuteromethanol one also obtains from clusters primarily deuterated cluster fragments in the photoionization mass spectrum (see Fig. 27). In addition, there are numerous molecular fragments, which are partially formed by fragmentation of doubly charged clusters. As a result, the mechanisms that lead to these fragments are different from those of single ionization, as is outlined in the following: The signal slope that corresponds to the products pair $(CH_3OD)D^+/((CH_3OD)_2D^+)$ is -1.50 ± 0.05 [188]. This slope of the PEPIPICO signal indicates that there is a primary fission process, were the primarily formed cluster dication is split into two singly charged cations. Subsequently, these decay into the observed fragments. The minimum cluster size that explains this slope is $(CH_3OD)_7^{++}$, where the cluster dication is initially split via fission into $(CH_3OD)_3^+ + (CH_3OD)_4^+$. Both cations decay subsequently via a deuteron transfer by the loss of CH_3O. In

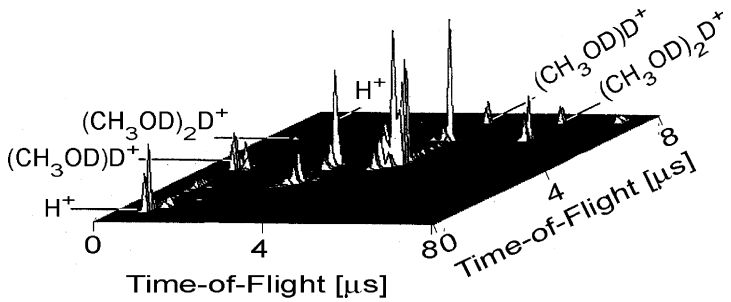

Fig. 26. Photoelectron–photoion–photoion coincidence (PEPIPICO) spectrum of *o*-deuteromethanol clusters. Experimental conditions: $E = 289$ eV; $T_0 = 300$ K; $p_0 = 2.4$ bar, seed gas: He [188].

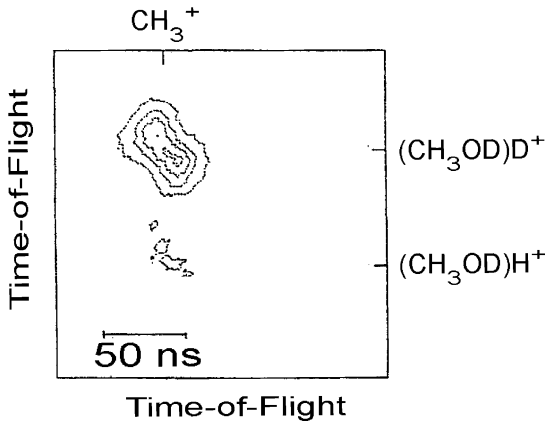

Fig. 28. Contour plot of the $CH_3^+/(CH_3OD)D^+$-coincidence obtained from the photoelectron–photoion–photoion coincidence (PEPIPICO) spectrum of *o*-deuteromethanol clusters. Experimental conditions: $E = 289$ eV; $T_0 = 300$ K; $p_0 = 2.4$ bar, seed gas: He [188].

addition, both monocations lose one and two neutral molecular moieties, respectively. The calculated signal slope of this fission mechanism is −1.46, which is in close agreement with the experimental slope [188]. The KER of this coincidence channel is 2.1 ± 0.5 eV, if the full size of the coincidence signal is analyzed. This corresponds to the minimum charge separation distance of 6.9 ± 2.1 Å, if exclusively electrostatic repulsion of the charges is considered. This distance is compatible with the size of a methanol cluster containing seven molecular moieties, indicating that there is charge separation in the doubly charged cluster prior to fission.

In addition, there are also molecular fragments, such as CH_3^+, CHO^+, and CH_2OD^+, which are correlated with deuterated cluster fragment ions. These cation pairs are already observed at moderate stagnation pressure ($p_0 \approx 1$ bar) with higher intensity than at increased p_0. This indicates that such fission channels come preferentially from small clusters, whereas cation pairs containing exclusively deuterated cluster cations dominate at higher p_0, i.e., they result from fission of larger clusters [188]. As one example, we briefly discuss the fission channel $CH_3^+/(CH_3OD)D^+$ (see Fig. 28), where the signal slope is -1.2 ± 0.05. Consistent with its occurrence in the small cluster regime is the fission mechanism that explains the shape of the PEPIPICO signal, starting at least from the trimer dication. After fission both singly charged cations, $(CH_3OD)^+ + (CH_3OD)_2^+$, undergo further stabilization, yielding the correlated products $CH_3^+/(CH_3OD)D^+$. Fragmentation of the methanol cation into $CH_3^+ + OD$ is expected to occur with high efficiency, since this route yields more stable products than the alternative route, where the charge is located on the other fragment (i.e., $OD^+ + CH_3$). The dimer cation is stabilized via a deuteron transfer yielding $(CH_3OD)D^+$, as discussed above. The kinetic energy release (KER) is obtained from the signal width perpendicular to the main diagonal of the PEPIPICO spectrum, where KER $= 2.9 \pm 0.5$ eV is found. This corresponds to a charge separation distance of 5.0 ± 1.0 Å, if a simple electrostatic point charge model is applied. The KER is also quite low, similar to the process discussed above, where protonated products are formed along with undetected neutrals, indicating that the charges are separated on different, i.e., not neighboring molecular sites.

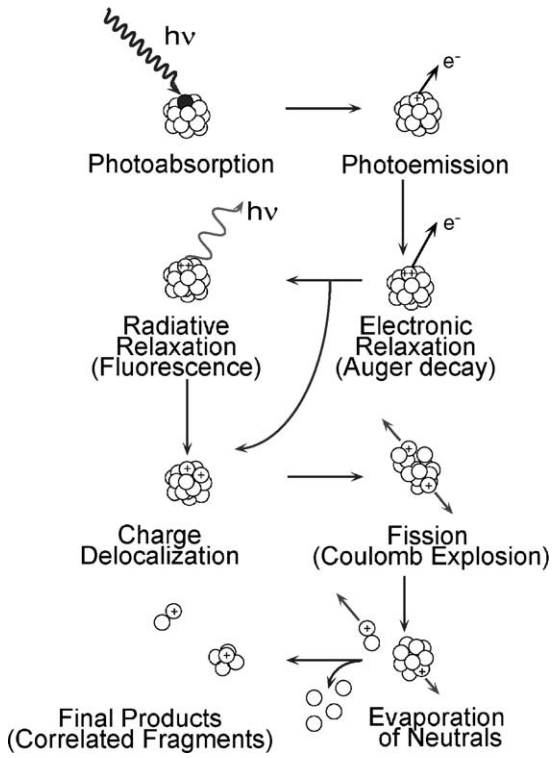

Fig. 29. Schematic diagram of the processes occurring after core level excitation in free atomic van der Waals clusters. Note that the fragmentation processes become more complicated in the case of molecular clusters, since various chemical fragmentation route may occur.

3.6. Mechanisms of cluster stabilization after core level excitation

The classical picture of the sequence of processes that occur after photoionization of clusters has been developed by Haberland [191]. This concept is mostly based on photoionization of outer electronic shells, where single ionization is dominant. Charge localization occurs in the picosecond time regime after excitation, so that dimers within a cluster are formed. The excess energy is thermalized and leads to fragmentation of the singly charged cluster.

In the case of core level excitation, the sequence of processes is more complicated. Fig. 29 shows a simple picture of the sequence of processes. The specificity of core level excitation is that the core hole is primarily stabilized either by electronic or radiative relaxation. The ratio between both relaxation processes depends on the excited atom, where heavy (high *Z*) elements relax preferably by the emission of X-rays, as outlined above in Section 3.4, whereas the core hole of light elements is stabilized by the emission of an Auger electron. Localization of the electronic relaxation pro-

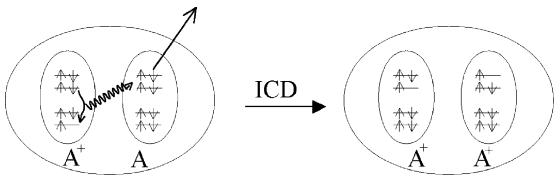

Fig. 30. Schematic diagram of the intracluster Coulomb decay (ICD leading to charge separation in clusters). The figure is adapted similar to results from [194,198]. The two upper levels correspond to the valence shell, the lower ones to inner-valence shell levels.

cesses leads to the expectation that a doubly charged atom is formed within the cluster, if the photoelectron and the Auger electron are directly emitted into the vacuum without ionizing neutral sites of the cluster. Triply charged clusters are formed, e.g., by a double Auger decay. The probability for an intra-cluster electron impact ionization process by a fast Auger electron was estimated for solid argon to be of the order of 18% [73,192]. Charge delocalization in clusters was discussed earlier in the context of radiative processes, where ultraviolet radiation is emitted as a result of the intermediate formation of charge transfer excimers [50]. The result of such processes is, that the charges a de-localized before fission, so that finally charge separation and losses of neutrals explain the final products that are detected by mass spectrometry and coincidence experiments.

A detailed view of the electronic decay mechanisms in weakly bound clusters has been developed from recent theoretical work, where various mechanisms of charge and energy transfer were considered [193]. The energy transfer process is schematically shown in Fig. 30. This represents a new, ultrafast mechanism of an intermolecular/interatomic Coulombic decay (ICD) [193–199], which is expected to occur in the 1–100 fs regime. Such a fast process implies that other competing processes are most likely of minor importance [199]. Therefore, charge transfer may occur, but it is expected to be of minor importance in weakly bound homogeneous clusters [193,198]. The energy transfer goes from the excited atom to a neighbor, where an outer-shell electron is emitted, so that the vacancies are located at different atoms in the cluster. This lowers the total energy of the cluster, where the Coulomb repulsion of the final hole states is shielded.

Recent experiments provide evidence for the ICD mechanism in 2s-excited neon clusters ($50\,\text{eV} \leq E \leq 60\,\text{eV}$) [200]. This photon energy regime is below the threshold of direct double ionization (atom: 62.53 eV [201], dimer: 60.9 eV [196]), so that this system is sensitive to energy transfer processes that lead to the emission of another electron. However, if dimers or larger clusters are present in the jet, then ICD can lead to the emission of an electron from an atom that neighbors the excited center. As a result, two singly charged atoms are formed at lower energy than corresponds to the atomic double ionization energy. We note that substantial lowering of the double ionization energies of free argon clusters relative to the free atom have been reported before [202]. One observes that the direct double ionization energies of free clusters are strongly size-dependent. They approach in the large cluster limit the double ionization energy of solid argon, which is known to be twice the work function [203].

High resolution photoelectron spectroscopy of neon clusters supports the ICD mechanism. Specifically, a low kinetic energy feature is found near 1.2 eV, which is independent on the primary excitation energy [200]. It is difficult to observe from the experimental point of view in solids and adsorbates, since low kinetic energy electrons occur in photoemission experiments as a result of inelastic scattering processes. Therefore, variable size clusters are ideal targets, since contributions from inelastic scattering can be easily varied by changing the expansion conditions, corresponding to changes in $\langle N \rangle$.

4. Conclusions and outlook

The field of core level excitation of free, variable size clusters has started to develop about a decade ago. Since then, numerous experiments on simple model systems have been performed. These showed, first of all, the feasibility of experiments in a spectral regime that suffers from low absorption cross sections and substantial linewidths of the electronic transitions. These drawbacks are more than compensated by various advantages, such as high selectivity for probing size effects of the local electronic and geometric structure as well as dynamic processes. The strength of core level excitation is well-known since many years from numerous studies on gaseous and condensed matter systems, where, e.g., EXAFS has become a standard approach for structural research. This state is still not reached for free clusters, where only a few investigations using EXAFS or multiple scattering have been performed to date. Size-dependent changes in geometric structure affect the electronic properties, which are also selectively probed by near-edge absorption as well as photoionization studies. This progress required substantial improvements of the radiation sources. State-of-the-art synchrotron radiation facilities including insertion devices, such as undulators, as well as soft X-ray monochromators play a key role for the progress in core level excitation experiments on free clusters. High brilliance, tunable radiation of small bandwidth is essential to observe small changes in electronic structure in clusters that change their size or composition. Current soft X-ray monochromators allow us to measure reliably energy shifts in the millielectronvolt regime. This can already be used to probe changes in rotational fine structure in molecules and molecular clusters [38]. The selectivity of core level spectroscopies has further increased since partial yield experiments have become successful [46,47]. Substantial progress in the understanding of nanoscopic systems including clusters that is based on core level spectroscopies appears to be possible. For example, technological important semiconductor clusters [112], de-

posited microclusters [204,205], as well as investigations on free nanoparticles represent fields of research that have just started to grow and give promising perspectives for future work in fundamental and applied research.

Future experiments that will contribute to an improved understanding of size effects of matter using short wavelength radiation will include size-selected clusters in the gas phase, which will be probed by core-level excitations. Current experiment in this field rely on ultraviolet radiation, so that only outer electronic shells can be investigated [206]. The use of soft X-rays for work on mass-selected clusters requires, however, stronger radiation sources, such as free electron lasers (FELs). These are not commonly available yet, but recent developments in this field already show the feasibility of this approach [207]. Recently, experiments on free clusters using a SASE-FEL in the vacuum ultraviolet regime already give a flavor, that novel research on free clusters can be pursued [208]. The time structure of SASE-FEL sources has also the advantage that pulsed cluster sources, such as laser evaporation [209], can be easier adapted to the tunable soft X-ray source than conventional synchrotron radiation. This is because the high repetition rate of synchrotron radiation sources requires stable cw-cluster sources over long time periods. Such cluster sources were not available during the last years, so that, e.g., experiments on free metal clusters were limited to low photon energies, where the absorption cross section was sufficiently high [15,210]. In addition, new concepts of synchrotron radiation sources, such as energy recovery linear accelerators (ERL) [211], as well as short pulse short wavelength laboratory sources, using, e.g., higher harmonics from femto- or attosecond lasers [212,213] and laser produced plasma radiation [214], will help to develop the field of core level excitation of clusters in the future.

Acknowledgements

It is a pleasure to thank all co-workers and collaborators, who have participated in this research during the last years. These are in alphabetical order among others: H. Baumgärtel, J. Blumberg, P.A. Dowben, W. Drube, R. Flesch, R. Frahm, J. Geiger, D. Gravel, C. Heinzel, A.P. Hitchock, H.W. Jochims, A. Knop, N. Kosugi, M. Kuhlmann, M. Lavollée, D.N. McIlroy, T. Möller, P. Morin, J.J. Neville, A.A. Pavlychev, C. Reynaud, H. Schmelz, D. Schwarz, M. Simon, C. Sonntag, W. Tappe, C.M. Teodorescu, and B. Wassermann. Financial support by the Deutsche Forschungsgemeinschaft, the Bundesministerium für Forschung und Technologie, and the Fonds der Chemischen Industrie are gratefully acknowledged.

References

[1] J. Jortner, Ber. Bunsenges. Phys. Chem. 88 (1984) 188; J. Jortner, Z. Phys. D 24 (1992) 247.
[2] (a) S. Sugano, H. Koizumi, Microcluster Physics, Springer, Berlin, 1998.; (b) T. Kondow, F. Mafuné, Progress in Experimental and Theoretical Studies of Clusters, Vol. 13, Adv. Ser. Phys. Chem., World Scientific, Singapore, 2003.
[3] H. Haberland (Ed.), Clusters of Atoms and Molecules, Vols. I and II, Springer Ser. Chem. Phys. Vols. 52 and 56, Springer, Berlin, 1994, 1995.
[4] J. Jortner, J. Chim. Phys. (Paris) 92 (1995) 205.
[5] F. Hache, D. Ricard, C. Flytzanis, U. Kreibig, Appl. Phys. A 47 (1988) 347.
[6] I.M.L. Billas, J.A. Becker, A. Chatelain, W.A. deHeer, Phys. Rev. Lett. 71 (1993) 4067.
[7] S.W. Chen, R.S. Ingram, M.J. Hostetler, J.J. Pietron, R.W. Murray, T.G. Schaaff, J.T. Khoury, M.M. Alvarez, R.L. Whetten, Science 280 (1998) 2098.
[8] W.A. deHeer, R. Martel, Phys. World 13 (2000) 49.
[9] C. Binns, Surf. Sci. Rep. 44 (2001) 1.
[10] H. Weller, Adv. Mater. 5 (1993) 88.
[11] J.R. Grover, E.A. Walters, J.K. Newman, M.G. White, J. Am. Chem. Soc. 107 (1985) 7329.
[12] E. Rühl, P.G.F. Bisling, B. Brutschy, H. Baumgärtel, Chem. Phys. Lett. 126 (1986) 232.
[13] T. Drewello, W. Krätschmer, M. Fieber-Erdmann, A. Ding, Int. J. Mass Spectrom. Ion Process. 124 (1993) R1.
[14] B. Bescos, H. Buchenau, R. Hoch, H.J. Schmidtke, G. Gerber, Chem. Phys. Lett. 285 (1988) 64.
[15] C. Brechignac, M. Broyer, Ph. Cahuzac, G. Delacretaz, P. Labastie, J.P. Wolf, L. Wöste, Phys. Rev. Lett. 60 (1988) 275.
[16] J. Farges, M.F. de Feraudy, B. Raoult, G. Torchet, J. Chem. Phys. 84 (1986) 3491.
[17] W.L. Jolly, K.D. Bomben, C.J. Eyermann, At. Data Nucl. Data Tables 31 (1984) 433.
[18] J. Stöhr, NEXAFS Spectroscopy, Springer Ser. Surf. Sci., Vol. 25, Springer, Berlin, 1992.
[19] K. Siegbahn, et al., ESCA Applied to Free Molecules, North-Holland, Amsterdam, 1971.
[20] A.P. Hitchcock, D.C. Mancini, J. Electron Spectrosc. Relat. Phenom. 67 (1994) 1.
[21] M. Drescher, M. Hentschel, R. Kienberger, M. Uiberacker, V. Yakovlev, A. Scrinizi, T. Westerwalbesloh, U. Kleineberg, U. Heinzmann, F. Krausz, Nature 419 (2002) 803.
[22] U. Becker, D.A. Shirley, VUV and Soft X-Ray Photoionization, Plenum Press, New York, 1996.
[23] B.K. Teo, D.C. Joy, in: K. Baberschke, D. Arvanitis (Eds.), EXAFS Spectroscopy, Plenum Press, New York, XAFS VIII, North-Holland, Amsterdam, 1995.
[24] E. Rühl, H.-W. Jochims, C. Schmale, E. Biller, A.P. Hitchcock, H. Baumgärtel, Chem. Phys. Lett. 178 (1991) 558.
[25] E.E. Koch (Ed.), Handbook of Synchrotron Radiation, North-Holland, Amsterdam, 1983.
[26] M. Lewerenz, B. Schilling, J.P. Toennies, Chem. Phys. Lett. 206 (1993) 381.
[27] O.F. Hagena, Z. Phys. D 4 (1987) 291.
[28] A.A. Vostrikov, D.Y. Dubov, I.V. Samoilov, Tech. Phys. 39 (1994) 1267.
[29] R. Karnbach, M. Joppien, J. Stapelfeldt, J. Wörmer, T. Möller, Rev. Sci. Instrum. 64 (1993) 2838.
[30] U. Buck, H. Meyer, Phys. Rev. Lett. 52 (1984) 109.
[31] E. Rühl, C. Schmale, H.W. Jochims, E. Biller, M. Simon, H. Baumgärtel, J. Chem. Phys. 95 (1991) 6544.
[32] E. Rühl, C. Heinzel, A.P. Hitchcock, H. Baumgärtel, J. Chem. Phys. 98 (1993) 2653.
[33] F. Federmann, O. Björneholm, A. Beutler, T. Möller, Phys. Rev. Lett. 73 (1994) 1549.
[34] E. Rühl, C. Heinzel, A.P. Hitchcock, H. Schmelz, C. Reynaud, H. Baumgärtel, W. Drube, R. Frahm, J. Chem. Phys. 98 (1993) 6820.

[35] E. Rühl, C. Heinzel, H. Baumgärtel, W. Drube, A.P. Hitchcock, Jpn. J. Appl. Phys. 32 (Suppl. 32-2) (1993) 791.
[36] O. Björneholm, F. Federmann, F. Fössing, T. Möller, Phys. Rev. Lett. 74 (1995) 3017.
[37] W. Kamke, B. Kamke, H.U. Kiefl, I.V. Hertel, J. Chem. Phys. 84 (1986) 1325.
[38] R. Flesch, W. Tappe, E. Rühl, A.A. Pavlychev, Surf. Rev. Lett. 9 (2002) 99.
[39] S. Kakar, O. Björneholm, J. Weigelt, A.R.B. de Castro, L. Tröger, R. Frahm, T. Möller, A. Knop, E. Rühl, Phys. Rev. Lett. 78 (1997) 1675.
[40] A. Knop, B. Wassermann, E. Rühl, Phys. Rev. Lett. 80 (1998) 2302.
[41] E. Rühl, S.D. Price, S. Leach, J. Phys. Chem. 93 (1989) 6312.
[42] E. Rühl, S.D. Price, S. Leach, J.H.D. Eland, Int. J. Mass Spectrom. Ion Process. 97 (1990) 175.
[43] E. Rühl, C. Heinzel, H. Baumgärtel, M. Lavollée, P. Morin, Z. Phys. D 31 (1994) 245.
[44] E. Rühl, A.P. Hitchcock, P. Morin, M. Lavollée, J. Chim. Phys. (Paris) 92 (1995) 521.
[45] U. Hergenhahn, A. Kolmakov, M. Riedler, A.R.B. de Castro, O. Löfken, T. Möller, Chem. Phys. Lett. 351 (2002) 235.
[46] O. Björneholm, Surf. Rev. Lett. 9 (2002) 3.
[47] M. Tchaplyguine, R. Feifel, R.R.T. Marinho, M. Gisselbrecht, S.L. Sorensen, A.N. de Brito, N. Martensson, S. Svensson, O. Björneholm, Chem. Phys. 289 (2003) 3.
[48] T. Baer, W.B. Peatman, E.W. Schlag, Chem. Phys. Lett. 4 (1969) 243.
[49] K. Müller-Dethlefs, E.W. Schlag, Ann. Rev. Phys. Chem. 42 (1991) 109.
[50] E. Rühl, C. Heinzel, H.-W. Jochims, Chem. Phys. Lett. 211 (1993) 403.
[51] J.H.D. Eland, Mol. Phys. 61 (1987) 725;
J.H.D. Eland, Acc. Chem. Res. 22 (1989) 381.
[52] M.G. White, J.R. Grover, J. Chem. Phys. 79 (1983) 4124.
[53] A.A. Pavlychev, E.V. Semenova, A.P. Hitchcock, E. Rühl, Physica B 208/209 (1995) 187.
[54] A.P. Hitchcock, E. Rühl, in: L.J. Dubé, J.B.A. Mitchell, J.W. McConkey, C.E. Brion (Eds.), The Physics of Electronic and Atomic Collisions, AIP Conference Proceedings, Vol. 360, American Institute of Physics, Woodbury, New York, 1995, p. 89.
[55] O. Björneholm, F. Federmann, F. Fössing, T. Möller, P. Stampfli, J. Chem. Phys. 104 (1996) 1846.
[56] O. Björneholm, F. Federmann, M. Joppien, F. Fössing, S. Kakar, R.v. Pietrowski, T. Möller, Surf. Rev. Lett. 3 (1996) 299.
[57] R. Haensel, G. Keitel, N. Kosuch, U. Nielsen, P. Schreiber, J. Phys. (Paris) 32 (C 4) (1971) 236.
[58] R. Haensel, N. Kosuch, U. Nielsen, U. Rössler, B. Sonntag, Phys. Rev. B 7 (1973) 1577.
[59] G. Johansson, J. Hedman, A. Berndtsson, M. Klasson, R. Nilsson, J. Electron Spectrosc. Relat. Phenom. 2 (1973) 295.
[60] O. Echt, D. Kreisle, E. Ecknagel, J.J. Saenz, R. Casero, J.M. Soler, Phys. Rev. A 38 (1988) 3236.
[61] A.M. Köhler, R. Reininger, V. Saile, G.L. Findley, Phys. Rev. A 33 (1986) 771.
[62] B.E. Springett, J. Jortner, M.H. Cohen, J. Chem. Phys. 48 (1968) 2720.
[63] M.R. Hoare, Adv. Chem. Phys. 40 (1979) 49.
[64] L. Resca, R. Resta, S. Rodriguez, Phys. Rev. B 18 (1978) 696;
L. Resca, R. Resta, S. Rodriguez, Phys. Rev. B 18 (1978) 702.
[65] R.E. Benfield, J. Chem. Soc., Faraday Trans. 88 (1992) 1107.
[66] A. Knop, E. Rühl, in: T. Kondow, K. Kaya, A. Terasaki (Eds.), Structure and Dynamic of Clusters, Universal Academic Press, Tokyo, 1996, p. 235.
[67] E. Rühl, Ber. Bunsenges. Phys. Chem. 96 (1992) 1172.
[68] J. Geiger, S. Rabe, C. Heinzel, H. Baumgärtel, E. Rühl, in: L.G. Christophorou, E. Illenberger, W.F. Schmidt (Eds.), Linking the Gaseous and Condensed Phases of Matter, Plenum Press, New York, 1994, p. 217.
[69] S. Kakar, O. Björneholm, O. Löfken, F. Federmann, A.V. Soldatov, T. Möller, Z. Phys. D 40 (1997) 84.
[70] A.A. Pavlychev, E. Rühl, J. Electron Spectrosc. Relat. Phenom. 106 (2000) 207;
A.A. Pavlychev, E. Rühl, J. Electron Spectrosc. Relat. Phenom. 107 (2000) 203.
[71] R. Flesch, A.A. Pavlychev, J.J. Neville, J. Blumberg, M. Kuhlmann, W. Tappe, F. Senf, O. Schwarzkopf, A.P. Hitchcock, E. Rühl, Phys. Rev. Lett. 86 (2001) 3767.
[72] E. Rühl, R. Flesch, W. Tappe, A.A. Pavlychev, J. Synchrotron Radiat. 8 (2001) 154.
[73] R. Scheuerer, P. Feulner, G. Rocker, Z. Lin, D. Menzel, DIET IV, in: G. Betz, P. Varga (Eds.), Springer Ser. Surf. Sci., Vol. 19, Springer, Berlin, 1990, p. 235.
[74] C.T. Chen, Y. Ma, F. Sette, Phys. Rev. A 40 (1989) 6737.
[75] L. Floreano, G. Natello, D. Cvetko, R. Gotter, M. Malvezzi, L. Marassi, A. Morgante, A. Santinello, A. Verdini, F. Tommasini, G. Tondello, Rev. Sci. Instrum. 70 (1999) 3855.
[76] R.A. Rosenberg, P.J. Love, P.R. La Roe, V. Rehn, C.C. Parks, Phys. Rev. B 31 (1985) 2634.
[77] K.P. Huber, G. Herzberg, Molecular Spectra and Molecular Structure, vol. 4, Van Nostrand, New York, 1979.
[78] O. Björneholm, F. Federmann, S. Kakar, T. Möller, J. Chem. Phys. 111 (1999) 546.
[79] G.R. Wright, C.E. Brion, J. Electron Spectrosc. Relat. Phenom. 4 (1974) 25.
[80] H. Shinohara, N. Nishi, N. Washida, J. Chem. Phys. 83 (1985) 1939;
U. Nagashima, H. Shinohara, N. Nishi, H. Tanaka, J. Chem. Phys. 84 (1986) 209.
[81] S. Myneni, Y. Luo, L.A. Näslund, M. Cavalleri, L. Öjamaäe, H. Ogasawara, A. Pelmenschikov, P. Wernet, P. Väterlein, C. Heske, Z. Hussain, L.G.M. Pettersson, A. Nilsson, J. Phys. Cond. Matter 14 (2002) L213.
[82] K.R. Wilson, M. Cavallieri, B.S. Rude, R.D. Schaller, A. Nilsson, L.G.M. Pettersson, N. Goldman, T. Catalano, J.D. Bozek, R.J. Saykally, J. Phys. Cond. Matter 14 (2002) L221.
[83] L. Triguero, L.G.M. Pettersson, H. Agren, Phys. Rev. B 58 (1998) 8097.
[84] L. Ojamäe, I. Shavitt, S.J. Singer, J. Chem. Phys. 109 (1998) 5547.
[85] I. Ishii, A.P. Hitchcock, J. Electron Spectrosc. Relat. Phenom. 46 (1988) 55.
[86] E. Rühl, B. Brutschy, H. Baumgärtel, Chem. Phys. Lett. 157 (1989) 379.
[87] C. Nowak, C. Rienecker, A. Kolmakov, J.O. Löfken, F. Picucci, M. Riedler, A.V. Soldatov, M. Wolff, T. Möller, J. Electron Spectrosc. Relat. Phenom. 103 (1999) 199.
[88] G.E. Yalovega, A.V. Soldatov, C. Nowak, M. Riedler, J.O. Löfken, A. Kolmakov, T. Möller, Phys. Solid State 42 (2000) 1942.
[89] M. Riedler, A.R.B. deCastro, A. Kolmakov, J.O. Löfken, C. Nowak, A.V. Soldatov, A. Wark, G. Yalovega, T. Möller, J. Chem. Phys. 115 (2001) 1319.
[90] M. Riedler, A.R.B. deCastro, A. Kolmakov, J.O. Löfken, C. Nowak, A.V. Soldatov, A. Wark, G. Yalovega, T. Möller, Phys. Rev. B 64 (2001) 245419.
[91] G. Yalovega, A.V. Soldatov, M. Riedler, M.R. Pederson, A. Kolmakov, C. Nowak, T. Möller, Chem. Phys. Lett. 356 (2002) 23.
[92] P.A. Akischin, N.G. Rambidi, Z. Phys. Chem. 213 (1960) 111.
[93] T.P. Martin, Phys. Rep. 95 (1983) 167.
[94] C.R. Natoli, EXAFS and Near Edge Structure, vol. 27, Springer, Berlin, 1983, p. 43.
[95] M. Kasrai, M.E. Fleet, G.M. Bancroft, K.H. Tan, J.M. Chen, Phys. Rev. B 43 (1991) 1763.
[96] M.-J. Malliavin, C. Coudray, J. Chem. Phys. 106 (1997) 2323.
[97] C. Ochsenfeld, R. Ahlrichs, J. Chem. Phys. 97 (1992) 3487.

[98] C.M. Teodorescu, D. Gravel, E. Rühl, J. Chem. Phys. 109 (1998) 9280.
[99] C.-M. Teodorescu, D. Gavel, J. Choi, D. Pugmire, P.A. Dowben, N. Fominykh, A.A. Pavlychev, E. Rühl, J. Electron Spectros. Relat. Phenom. 101–103 (1999) 193.
[100] E. Rühl, R. Flesch, W. Tappe, D. Novikov, N. Kosugi, J. Chem. Phys. 116 (2002) 3316.
[101] T.P. Martin, J. Chem. Phys. 81 (1984) 4426.
[102] N. Kosugi, E. Shigemasa, A. Yagishita, Chem. Phys. Lett. 190 (1992) 481.
[103] A. Yagishita, E. Shigemasa, N. Kosugi, Phys. Rev. Lett. 72 (1994) 3961.
[104] T. Hayakawa, K. Nagaya, K. Hamada, Y. Ohmasa, M. Yao, J. Phys. Soc. Jpn. 69 (2000) 2850.
[105] D. Gravel, Ph.D. Thesis, University of Osnabrück, 2003.
[106] J. Berkowitz, J.R. Marquart, J. Chem. Phys. 39 (1963) 275; J.R. Marquart, J. Berkowitz, J. Chem. Phys. 39 (1963) 283.
[107] W.H.E. Schwarz, Chem. Phys. 11 (1975) 217.
[108] K. Raghavachari, C. McMichael Rohlfing, J.S. Binkley, J. Chen. Phys. 93 (1990) 5862.
[109] G.E. Quelch, H.F. Schaefer III, C.J. Marsden, J. Am. Chem. Soc. 112 (1990) 8719.
[110] B.C. Pan, C.K. Duan, S.D. Xia, C.Y. Xiao, Phys. Rev. B 50 (1994) 17556.
[111] P. Lenain, E. Picquenard, J. Corset, D. Jensen, R. Steudel, Ber. Bunsenges. Phys. Chem. 92 (1988) 859.
[112] C. Nowak, H. Döllefeld, A. Eychmüller, J. Friedrich, A. Kolmakov, J.O. Löfken, M. Riedler, A. Wark, H. Weller, M. Wolff, T. Möller, J. Chem. Phys. 114 (2001) 489.
[113] D. Schwarz, Thesis, Universität Osnabrück, 1999.
[114] J. Lüning, J. Rockenberger, S. Eisebitt, J.-E. Rubensson, A. Karl, A. Kornowski, H. Weller, W. Eberhardt, Solid State Commun. 112 (1999) 5.
[115] R. Buczko, G. Duscher, S.J. Pennycook, S.T. Pantelides, Phys. Rev. Lett. 85 (2000) 2168.
[116] S.J. Lippard, J.M. Berg, Principles of Bioinorganic Chemistry, University Science Books, Mill Valley, 1994.
[117] D. Gravel, M. Kuhlmann, D. Schwarz, J. Blumberg, C.M. Teodorescu, E. Rühl, BESSY Annual Report, Berlin, 1998, p. 187.
[118] B.W. van de Waal, J. Chem. Phys. 90 (1989) 3407.
[119] J.W. Lee, G.D. Stein, J. Phys. Chem. 91 (1987) 2450.
[120] W. Malzfeldt, W. Niemann, P. Rabe, R. Haensel, Springer Proc. Phys. 2 (1984) 445; W. Malzfeldt, Ph.D. Thesis, University of Kiel, 1985.
[121] J. Mustre, Y. Jacoby, E.A. Stern, J.J. Rehr, Phys. Rev. B 42 (1990) 10483; J.J. Rehr, R.C. Albers, S.I. Zabinsky, Phys. Rev. Lett. 69 (1992) 3397; E.A. Stern, M. Newville, B. Ravel, Y. Yacoby, D. Haskel, Physica B 208/209 (1995) 117.
[122] M. Thomas, Optical Grapher Program, Center of X-Ray Optics, U.C. Berkeley.
[123] W. Niemann, W. Malzfeldt, P. Rabe, R. Haensel, M. Lübcke, Phys. Rev. B 35 (1987) 1099.
[124] B.W. van de Waal, Z. Phys. D 20 (1991) 349.
[125] B.W. van de Waal, J. Chem. Phys. 98 (1993) 4909.
[126] B.W. van de Waal, Phys. Rev. Lett. 76 (1996) 1083.
[127] E.G. Cox, Rev. Mod. Phys. 30 (1958) 159.
[128] G. Karlström, P. Linse, A. Wallqvist, B. Jönsson, J. Am. Chem. Soc. 105 (1983) 3777.
[129] V. Spirko, O. Engvist, P. Soldan, H.L. Selzle, E.W. Schlag, P. Hobza, J. Chem. Phys. 111 (1999) 572.
[130] K.S. Law, M. Schauer, E.R. Bernstein, J. Chem. Phys. 81 (1984) 4871.
[131] P. Hobza, H.L. Selzle, E.W. Schlag, J. Am. Chem. Soc. 116 (1994) 3500.
[132] K.O. Börnsen, H.L. Selzle, E.W. Schlag, J. Chem. Phys. 85 (1986) 1726.
[133] S.L. Price, A.J. Stone, J. Chem. Phys. 86 (1987) 2859.
[134] K. Nagaya, M. Yao, T. Hayakawa, Y. Ohmasa, Y. Kajihara, M. Ishii, Y. Katayama, Phys. Rev. Lett. 89 (2002) 243401.
[135] J. Becker, K. Rademann, F. Hensel, Z. Naturforsch. A 46 (1991) 453.
[136] D. Hohl, R.O. Jones, R. Car, M. Parrinello, Chem. Phys. Lett. 139 (1987) 540.
[137] S. Kohara, A. Goldbach, N. Koura, M.L. Saboungi, L.A. Curtiss, Chem. Phys. Lett. 287 (1998) 282.
[138] M. Cardona, L. Ley (Eds.), Photoemission in Solids I: General Principles, Springer, Berlin, 1978.
[139] J.C. Fuggle, N. Martensson, J. Electron Spectrosc. Relat. Phenom. 21 (1980) 275.
[140] A. Knop, H.W. Jochims, A.L.D. Kilcoyne, A.P. Hitchcock, E. Rühl, Chem. Phys. Lett. 223 (1994) 553.
[141] L. Pettersson, J. Nordgren, L. Selander, C. Nordling, K. Siegbahn, H. Agren, J. Electron Spectrosc. Relat. Phenom. 27 (1982) 29.
[142] P. Stampfli, K.H. Bennemann, Ber. Bunsenges. Phys. Chem. 96 (1992) 1243.
[143] W. Wurth, G. Rocker, P. Feulner, R. Scheuerer, L. Zhu, D. Menzel, Phys. Rev. B 47 (1993) 6697.
[144] M. Altarelli, W. Andreoni, F. Bassani, Solid State Commun. 16 (1975) 143.
[145] K. Müller-Dethlefs, E.W. Schlag, Ann. Rev. Phys. Chem. 42 (1991) 109.
[146] W. Habenicht, K. Müller-Dethlefs, E.W. Schlag, J. Electron Spectrosc. Relat. Phenom. 52 (1990) 697.
[147] A. Niehaus, J. Phys. B 10 (1977) 1845.
[148] H. Hanashiro, Y. Suzuki, T. Sasaki, A. Mikuni, T. Takayanagi, K. Wakiya, H. Suzuki, A. Danjo, T. Hino, S. Ohtani, J. Phys. B 12 (1979) L775.
[149] K. Helenelund, S. Hedman, L. Asplund, U. Gelius, K. Siegbahn, Phys. Scr. 27 (1983) 245.
[150] A. Russek, W. Mehlhorn, J. Phys. B 19 (1986) 911.
[151] P.A. Heimann, D.W. Lindle, T.A. Ferrett, S.H. Liu, L.J. Medhurst, M.N. Piancastelli, D.A. Shirley, U. Becker, H.G. Kerkhoff, B. Langer, D. Szostak, R. Wehlitz, J. Phys. B 20 (1987) 5005.
[152] P.v.d. Straten, R. Morgenstern, A. Niehaus, Z. Phys. D 8 (1988) 35.
[153] W. Eberhardt, S. Bernstorff, H.W. Jochims, S.B. Whitfield, B. Crasemann, Phys. Rev. A 38 (1988) 3808.
[154] J. Tulkki, T. Aberg, S.B. Whitfield, B. Crasemann, Phys. Rev. A 41 (1990) 181.
[155] J. Mursu, H. Aksela, O.-P. Sairanen, A. Kivimäki, E. Nommiste, A. Ausmees, S. Svensson, S. Aksela, J. Phys. B 29 (1996) 4387.
[156] I.L. Bradeanu, R. Flesch, E. Rühl, in preparation.
[157] B. Kassühlke, P. Averkamp, S. Frigo, P. Feulner, W. Berthold, Phys. Rev. B 55 (1997) 10854.
[158] G. Kutluk, T. Takaku, M. Kanno, T. Nagata, E. Shigemasa, A. Yagishita, F. Koike, J. Phys. B 27 (1994) 5637.
[159] B. Kassühlke, Ph.D. Thesis, Technische Universität München, Munich, 1999.
[160] E. Rühl, A. Knop, A.P. Hitchcock, P.A. Dowben, D.N. McIlroy, Surf. Rev. Lett. 3 (1996) 557.
[161] G. Rocker, P. Feulner, R. Scheuerer, L. Zhu, D. Menzel, Phys. Scr. 41 (1990) 1014.
[162] H. Aksela, S. Aksela, H. Pulkkinen, G.M. Bancroft, K.H. Tan, Phys. Rev. A 37 (1988) 1798.
[163] M. Meyer, E.v. Raven, B. Sonntag, J.E. Hansen, Phys. Rev. A 43 (1991) 177.
[164] J. Wörmer, M. Joppien, G. Zimmerer, T. Möller, Phys. Rev. Lett. 67 (1991) 2053.
[165] J. Wörmer, R. Karnbach, M. Joppien, T. Möller, J. Chem. Phys. 104 (1996) 8269.

[166] R. Flesch, H.-W. Jochims, J. Plenge, E. Rühl, Phys. Rev. A 61 (2000) 62504.
[167] M. Meyer, A. Marquette, A. Grum-Grzhimailo, R. Flesch, E. Rühl, Surf. Rev. Lett. 9 (2002) 141.
[168] C. Cachoncinlle, J.M. Pouvesle, F. Davanloo, J.J. Coogan, C.B. Collins, Opt. Commun. 79 (1990) 41;
C. Cachoncinlle, J.M. Pouvesle, F. Davanloo, J.J. Coogan, C.B. Collins, J. Phys. D 23 (1990) 984.
[169] G. Klein, M.J. Carvalho, J. Phys. B 14 (1981) 1283.
[170] A. Ulrich, H.J. Körner, W. Krötz, G. Ribitzki, D.E. Murnick, E. Matthias, P. Kienle, D.H.H. Hoffmann, J. Appl. Phys. 63 (1987) 357.
[171] H. Langhoff, Opt. Commun. 68 (1988) 31.
[172] H. Langhoff, J. Phys. B 27 (1994) L709.
[173] N. Saito, I.H. Suzuki, Int. J. Mass Spectrom. Ion Process. 115 (1992) 157.
[174] J.H.D. Eland, in: C.Y. Ng (Ed.), Vacuum Ultraviolet Photoionization and Photodissociation of Molecules and Clusters, World Scientific, Singapore, 1991, p. 297.
[175] P. Scheier, T.D. Märk, J. Chem. Phys. 86 (1987) 3056.
[176] M. Simon, Ph.D. Thesis, Université de Paris-Sud, Orsay, 1992.
[177] P. Scheier, T.D. Märk, Chem. Phys. Lett. 136 (1987) 423.
[178] W. Tappe, R. Flesch, E. Rühl, R. Hoekstra, T. Schlathölter, Phys. Rev. Lett. 88 (2002) 143401.
[179] A. Niehaus, J. Phys. B 19 (1986) 2925.
[180] T. Schlathölter, R. Hoekstra, R. Morgenstern, J. Phys. B 31 (1998) 1321.
[181] S. Martin, L. Chen, A. Denis, J. Desesquelles, Phys. Rev. A 57 (1998) 4518.
[182] J. Opitz, H. Lebius, B. Saint, S. Jacquet, B.A. Huber, H. Cederquist, Phys. Rev. A 59 (1999) 3562.
[183] B. Walch, C.L. Cocke, R. Voelpel, E. Salzborn, Phys. Rev. Lett. 72 (1994) 1439.
[184] F. Chandezon, C. Guet, B.A. Huber, D. Jalabert, M. Maurel, E. Monnand, C. Ristori, J.C. Rocco, Phys. Rev. Lett. 74 (1995) 3784.
[185] C. Guet, X. Biquard, P. Blaise, S.A. Blundell, M. Gross, B.A. Huber, D. Jalabert, M. Maurel, L. Plagne, J.C. Rocco, Z. Phys. D 40 (1997) 317.
[186] L. Plagne, C. Guet, Phys. Rev. A 59 (1999) 4461.
[187] P. Scheier, A. Stamatovic, T.D. Märk, J. Chem. Phys. 88 (1988) 4289.
[188] J. Geiger, E. Rühl, Int. J. Mass Spectrom. 200 (2002) 99.
[189] K.D. Cook, G.G. Jones, J.W. Taylor, Int. J. Mass Spectrom. Ion Phys. 35 (1980) 273.
[190] S.V. Olesik, J.W. Taylor, Int. J. Mass Spectrom. Ion Phys. 57 (1984) 315.
[191] H. Haberland, Surf. Sci. 156 (1985) 303.
[192] K.B. McAfee Jr., R.S. Hozack, Phys. Rev. A 32 (1985) 810.
[193] J. Zobeley, R. Santra, L.S. Cederbaum, J. Chem. Phys. 115 (2001) 5076.
[194] L.S. Cederbaum, J. Zobeley, F. Tarantelli, Phys. Rev. Lett. 79 (1997) 4778.
[195] J. Zobeley, L.S. Cederbaum, F. Tarantelli, J. Phys. Chem. A 103 (1999) 11145.
[196] R. Santra, J. Zobeley, L.S. Cederbaum, N. Moiseyev, Phys. Rev. Lett. 85 (2000) 4490.
[197] R. Santra, J. Zobeley, L.S. Cederbaum, Phys. Rev. B 64 (2001) 245104.
[198] R. Santra, L.S. Cederbaum, Phys. Rep. 368 (2002) 1.
[199] R. Santra, L.S. Cederbaum, Phys. Rev. Lett. 90 (2003) 153401.
[200] S. Marburger, O. Kugeler, U. Hergenhahn, T. Möller, Phys. Rev. Lett. 90 (2003) 203401.
[201] K. Harth, M. Raab, H. Hotop, Z. Phys. D 7 (1987) 213;
W. Persson, Phys. Scr. 3 (1971) 133.
[202] E. Rühl, C. Schmale, H.C. Schmelz, H. Baumgärtel, Chem. Phys. Lett. 191 (1992) 430.
[203] H.W. Biester, M.J. Besnard, G. Dujardin, L. Hellner, E.E. Koch, Phys. Rev. Lett. 59 (1987) 1277.
[204] J.T. Lau, A. Achleiter, W. Wurth, Chem. Phys. Lett. 317 (2000) 269.
[205] J. Bansmann, V. Senz, R.P. Methling, R. Rohlsberger, K.H. Meiwes-Broer, Mater. Sci. Eng. C 19 (2002) 305.
[206] J. Ho, K.M. Erwin, W.C. Lineberger, J. Chem. Phys. 93 (1990) 6987;
G. Ganteför, H.R. Siekmann, H.O. Lutz, K.H. Meiwes-Broer, Chem. Phys. Lett. 165 (1990) 293.
[207] J. Andruszkow, et al., Phys. Rev. Lett. 85 (2000) 3825.
[208] H. Wabnitz, L. Bittner, A.R.B. de Castro, R. Dohrmann, P. Gürtler, T. Laarmann, W. Laasch, J. Schulz, A. Swiderski, K. von Haeften, T. Möller, B. Faatz, A. Fateev, J. Feldhaus, C. Gerth, U. Hahn, E. Saldin, E. Schneidmiller, K. Stychev, K. Tiedtke, R. Treusch, M. Yukov, Nature 420 (2002) 482.
[209] S. Maruyama, L.R. Anderson, R.E. Smalley, Rev. Sci. Instrum. 61 (1990) 3686.
[210] C. Brechignac, M. Broyer, P. Cahuzac, G. Delacretaz, P. Labastie, L. Wöste, Chem. Phys. Lett. 120 (1985) 559;
J. Blanc, M. Broyer, P. Dugourd, P. Labastie, M. Sence, J.P. Wolf, L. Wöste, J. Chem. Phys. 102 (1995) 680.
[211] S.M. Gruner, D. Bilderback, I. Bazarov, K. Finkelstein, G. Krafft, L. Merminga, H. Padamsee, Q. Shen, C. Sinclair, M. Tigner, Rev. Sci. Instrum. 73 (2002) 1402.
[212] R. Bartels, S. Backus, E. Zeek, L. Misoguti, G. Vdovin, I.P. Christov, M.M. Murnane, H.C. Kapteyn, Nature 406 (2000) 164.
[213] L. Nugent-Glandorf, M. Scheer, D.A. Samuels, V.M. Bierbaum, S.R. Leone, J. Chem. Phys. 117 (2002) 6108.
[214] J.P. Mosnier, J. Costello, E. Kennedy, W. Whitty, J. Phys. B 33 (2000) 5203.